U.K. HiGEM: The New U.K. High-Resolution Global Environment Model—Model Description and Basic Evaluation

L. C. SHAFFREY,* I. STEVENS,+ W. A. NORTON,* M. J. ROBERTS,#,@ P. L. VIDALE,*,# J. D. HARLE,& A. JRRAR,** D. P. STEVENS,+ M. J. WOODAGE,++ M. E. DEMORY,*,# J. DONNERS,*,# D. B. CLARK,## A. CLAYTON,#,@ J. W. COLE,* S. S. WILSON,*,@ W. M. CONNOLLEY,** T. M. DAVIES,@@ A. M. IWI,&& T. C. JOHNS,@ J. C. KING,** A. L. NEW,& J. M. SLINGO,* A. SLINGO,++ L. STEENMAN-CLARK,* AND G. M. MARTIN@

* *National Centre for Atmospheric Science, Department of Meteorology, University of Reading, Reading, United Kingdom*
+ *School of Mathematics, University of East Anglia, Norwich, United Kingdom*
# *United Kingdom–Japan Climate Collaboration, Earth Simulator Centre, Yokohama, Japan*
@ *Met Office Hadley Centre for Climate Prediction and Research, Exeter, United Kingdom*
& *National Oceanography Centre Southampton, University of Southampton, Southampton, United Kingdom*
** *British Antarctic Survey, Cambridge, United Kingdom*
++ *Environmental Systems Science Centre, University of Reading, Reading, United Kingdom*
Centre for Ecology and Hydrology, Wallingford, United Kingdom
@@ *Met Office, Exeter, United Kingdom*
&& *British Atmospheric Data Centre, Rutherford Appleton Laboratory, Chilton, United Kingdom*

(Manuscript received 4 March 2008, in final form 30 June 2008)

ABSTRACT

This article describes the development and evaluation of the U.K.'s new High-Resolution Global Environmental Model (HiGEM), which is based on the latest climate configuration of the Met Office Unified Model, known as the Hadley Centre Global Environmental Model, version 1 (HadGEM1). In HiGEM, the horizontal resolution has been increased to 0.83° latitude × 1.25° longitude for the atmosphere, and 1/3° × 1/3° globally for the ocean. Multidecadal integrations of HiGEM, and the lower-resolution HadGEM, are used to explore the impact of resolution on the fidelity of climate simulations.

Generally, SST errors are reduced in HiGEM. Cold SST errors associated with the path of the North Atlantic drift improve, and warm SST errors are reduced in upwelling stratocumulus regions where the simulation of low-level cloud is better at higher resolution. The ocean model in HiGEM allows ocean eddies to be partially resolved, which dramatically improves the representation of sea surface height variability. In the Southern Ocean, most of the heat transports in HiGEM is achieved by resolved eddy motions, which replaces the parameterized eddy heat transport in the lower-resolution model. HiGEM is also able to more realistically simulate small-scale features in the wind stress curl around islands and oceanic SST fronts, which may have implications for oceanic upwelling and ocean biology.

Higher resolution in both the atmosphere and the ocean allows coupling to occur on small spatial scales. In particular, the small-scale interaction recently seen in satellite imagery between the atmosphere and tropical instability waves in the tropical Pacific Ocean is realistically captured in HiGEM. Tropical instability waves play a role in improving the simulation of the mean state of the tropical Pacific, which has important implications for climate variability. In particular, all aspects of the simulation of ENSO (spatial patterns, the time scales at which ENSO occurs, and global teleconnections) are much improved in HiGEM.

1. Introduction

This paper is the first in a series describing the development and performance of the U.K.'s first High-Resolution Global Environmental Model (HiGEM). These papers will highlight different aspects of the earth system and the new perspectives that high resolution has brought to the simulation of the coupled system. The HiGEM project is a partnership between the Natural Environment Research Council (NERC), the U.K. academic community, and the Met Office Hadley Centre. Its aim is to extend the latest climate configuration of the Met Office Hadley Centre Global

Corresponding author address: Dr. Len C. Shaffrey, NCAS Climate, Department of Meteorology, University of Reading, Reading RG6 6BB, United Kingdom.
E-mail: l.c.shaffrey@reading.ac.uk

DOI: 10.1175/2008JCLI2508.1

Environmental Model version 1 (HadGEM1) to higher resolution in both the atmosphere and ocean. HiGEM has also formed the core of the modeling activities of the United Kingdom–Japan Climate Collaboration (UJCC) between the National Centre for Atmospheric Science, the Met Office Hadley Centre, and the Earth Simulator Centre, in which U.K. staff are permanently based at the Earth Simulator Centre in Yokohama, Japan.

HiGEM represents a significant change in how global environment modeling is conducted in the United Kingdom; it brings together the fundamental research within NERC and the academic community with the climate prediction program of the Met Office Hadley Centre. HiGEM has facilitated the engagement of NERC expertise in various aspects of climate system science with the development and evaluation of the U.K.'s next-generation model of the global environment. For the first time, many of the principal areas of NERC science are working together, leading to a concerted effort in state-of-the-art global environment modeling that hitherto has been somewhat fragmented. Moving toward a higher resolution has enabled the gap to be narrowed between modelers and scientists specializing in particular processes and phenomena, and between models and observations of the earth system.

The overarching drivers for the development of HiGEM are, first, to explore the impact of higher resolution on the fidelity of the simulations, and, second, to understand the nonlinear processes that give rise to interactions between small and large spatial scales, and between high and low frequencies, within the climate system. Complex fluid flows in the atmosphere and oceans are a fundamental feature of the climate system. They transport energy, tracers, and momentum within and between system components; they occur over a wide range of spatial scales and evolve over a wide range of time scales. A clear imperative is to develop models of much a higher resolution, in order to simulate flows explicitly down to smaller scales, and to capture potential nonlinear interactions between a wider ranger of spatial and temporal scales and between different components of the climate system. Rapid increases in computer power are enabling much higher resolutions to be used, and HiGEM attempts to exploit those opportunities.

The current, state-of-the-art coupled climate models used in the Intergovernmental Panel on Climate Change (IPCC) Fourth Assessment Report (AR4; Solomon et al. 2007) have a typical resolution of approximately1.5°–3° in the atmosphere and ~1° in the ocean. In neither component are some key aspects of the climate system (such as the influence of ocean eddies, orographic forcing of the atmosphere, tropical cyclones) adequately represented. As computing power has increased during the 40-yr history of weather and climate modeling, the horizontal resolution of numerical weather prediction models has increased by a few orders of magnitude. The horizontal resolution of climate models has not increased by such a degree, and instead the increase in computing power has been used almost exclusively to introduce more complex parameterizations and additional processes, to perform multicentury integrations, and, more recently, to explore uncertainty through large ensembles of simulations.

However, there is a strong case for a higher resolution to be used in all components of the coupled system. For the atmosphere, high-resolution simulations have already demonstrated significant improvements in the representation of storm-track processes and of the detailed precipitation distribution over Europe where orographic effects are important (Pope and Stratton 2002; Jung et al. 2006). For the ocean, there is good evidence that eddy-permitting models provide a much better representation of the wind-driven circulation and western boundary currents (Semtner and Chervin 1988; Bryan and Holland 1989; FRAM Group 1991; Semtner and Chervin 1992). The early eddy-permitting models also captured, for the first time, the geographical distribution of mesoscale eddy variability observed by satellite altimeters. Because the equatorial Rossby radius for ocean waves is of the order of 100–250 km (e.g., Gill 1982), it is clear that a higher resolution will also give a more accurate simulation of equatorial waves, which are a key part of El Niño. However, there are still deficiencies at mid- to high latitudes where the Rossby deformation radius remains unresolved, indicating a need for even higher resolution (Smith et al. 2000).

At the land surface, strong variations in properties such as topographic height, vegetation cover, soil properties, soil moisture, and snow cover occur at all length scales. These combine nonlinearly to produce large variations in surface fluxes of heat, moisture, momentum, and carbon dioxide. As a result, the modeling of surface processes in GCMs is strongly constrained by horizontal resolution. Numerous studies have illustrated that land surface feedbacks can affect the atmosphere at scales from the local up to the global (e.g., Taylor et al. 2007). Explicitly resolving finer-scale surface features should lead to improvements in the simulation of climate over continental regions.

Sea ice is highly inhomogeneous, with much of the exchange of heat between the ocean and atmosphere taking place over small areas of open water (leads and polynyas) within the ice cover. These exchanges of heat determine the overall growth of the winter sea ice and

the consequent modification of ocean water masses through brine rejection. Correct parameterization of these energy exchanges is essential for realistic climate simulations and requires high-resolution atmospheric and oceanic fields in order to calculate the fraction of open water and its distribution within a grid cell correctly. The rheology of sea ice is also highly nonlinear, and thus the simulation of ice–ocean interactions requires a high spatial resolution (Holland 2001).

High-resolution simulations of the climate system have generally been run in uncoupled mode, and often only at a regional scale where the simulation may be compromised by errors in the boundary forcing. The impact of details in the structures may be substantial. For example, results from a coupled model have shown a dramatic improvement in the mean tropical climate and the simulation of El Niño when the atmosphere is run at a resolution commensurate with that of the ocean (Guilyardi et al. 2004). Furthermore, analyses of near-surface wind speed and direction over the global ocean from the Quick Scatterometer (QuikSCAT) satellite radar scatterometer (Chelton et al. 2004) have shown persistent small-scale features that are indicative of air–sea interaction over sea surface temperature fronts, such as the Gulf Stream, and the influence of islands and coastal mountains. Similarly, results from a high-resolution version of the coupled Model for Interdisciplinary Research on Climate 3.2 (MIROC3.2; K-1 Model Developers 2004) show that resolving small-scale islands and orographic features, such as the Hawaiian Islands, can have far-reaching effects on the atmosphere and ocean (Sakamoto et al. 2004)

This paper describes the development of HiGEM, and presents a basic evaluation of its performance from a multidecadal integration for the current climate. Further papers will cover in more detail aspects such as weather, ocean variability, and modes of climate variability (Roberts et al. 2009; Shaffrey et al. 2009, unpublished manuscript; D. P. Stevens et al. 2009, unpublished manuscript). Section 2 contains a description of HiGEM, including the changes made from HadGEMl, the production of the high-resolution boundary conditions, and the optimization of the code. Using results from a multidecadal simulation for the current climate, the performance of the full system and of each component of the model is described in section 3, with a particular emphasis on the impact of high resolution on the simulation. Section 4 highlights specific coupled ocean–atmosphere interactions that are facilitated by high resolution in both the atmosphere and ocean combined. The paper concludes with some discussion and overall conclusions concerning model performance.

2. Model description

HiGEM is based on the latest climate configuration of the Met Office Unified Model, HadGEM1 (Johns et al. 2006; Martin et al. 2006; Ringer et al. 2006), which contributed to the IPCC Fourth Assessment Report (Solomon et al. 2007). The horizontal resolution of HadGEM1 is 1.25° latitude × 1.875° longitude (N96) in the atmosphere, and 1° × 1° (increasing to 1/3° meridionally near the equator) in the ocean.

In HiGEM, the horizontal resolution has been increased to 0.83° latitude × 1.25° longitude (N144) for the atmosphere, and 1/3° × 1/3° globally for the ocean and sea ice. Experience in numerical weather prediction suggests that as the resolution is increased, then weather systems, the building blocks of climate, are more realistically represented (Jung et al. 2006). Similarly, experience with high-resolution ocean models suggests that at 1/3° ocean resolution, small-scale eddies are represented (particularly at low latitudes), steep gradients such as in western boundary currents are better resolved, and the ocean can be made much less diffusive (Roberts et al. 2004). HiGEM has a higher resolution in both components than has hitherto been used in the United Kingdom for extended simulations of the coupled global environment.

In the development of HiGEM, a number of versions of the model were produced. In this paper we describe HiGEM1.2 and document the changes required to produce this model from HadGEM1. An earlier version of HiGEM, HiGEM1.1 was also extensively tested and a centennial simulation was run on the Earth Simulator. This integration will be described in greater detail in Roberts et al. (2009).

The move to higher resolution has necessitated some changes to the model, particularly in the ocean. Furthermore, since the submission to the IPCC Fourth Assessment Report, various improvements have been implemented in HadGEM1 to form the latest version, HadGEM2-Atmosphere–Ocean (AO). Some of these improvements have been included in the HiGEM code.

a. Atmosphere component

The atmosphere component of HiGEM1.2 is very similar to that of HadGEM1 (see Martin et al. 2006). It has a nonhydrostatic dynamical core (Davies et al. 2005), with semi-Lagrangian transport. Discretization is on an Arakawa C grid. Parameterizations in HadGEM1 are substantially improved, for example, with new boundary layer and convection schemes, compared to the earlier Met Office Hadley Centre's third generation climate model (HadCM3) (Gordon et al. 2000). HadGEM1 includes an interactive aerosol

scheme, driven by surface and elevated emissions. Both HadGEMl and HiGEM1.2 have 38 levels in the vertical. The top of both models is at 39 km, implying the stratosphere is not well resolved in HadGEM1 and HiGEM1.2.

With the increased horizontal resolution of HiGEM1.2 the time step was reduced from 30 (HadGEM1 value) to 20 min. The magnitude of polar filtering in the advection scheme was also reduced. In HadGEM1 a moisture diffusion scheme was implemented to prevent numerical instabilities, known as gridpoint storms (e.g., Emanuel 1994), which involve a feedback between the resolved vertical velocity and parameterized diabatic processes. The vertical velocity threshold at which the targeted moisture diffusion is triggered was increased from 0.l m s^{-1} in HadGEM1 to 0.4 m s^{-1} in HiGEM1.2.

Two changes in the physical parameterizations implemented in HadGEM2-AO were also found to have a beneficial impact on the simulation in HiGEM1.2, and so they were included. These included reducing the snow-free sea ice albedo from 0.61 to 0.57 and changing the treatment of runoff over frozen soil. In HadGEM1 it was assumed that none of the runoff penetrated into frozen soil. When this assumption was relaxed there was marked improvement in the seasonal cycle of soil moisture and land temperatures. HiGEM1.2 includes the total ocean current in the calculation of the surface fluxes of moisture, heat, and momentum. This produces improvements in the simulation of sea surface temperatures in the tropical east Pacific compared to HadGEM1 where the ocean currents were not included in the calculation of surface fluxes. The coupling frequency is unchanged from HadGEM1,that is, that ocean and atmosphere are coupled once per day.

b. Ocean component

The ocean component follows that used in the ocean component of HadGEM1 (Johns et al. 2006), but with increased horizontal resolution and improvements to some of the model physics. HadGEM1 and HiGEM1.2 are based on the Met Office Unified Model in which the ocean component is formulated on a spherical latitude–longitude grid, which has a singularity at the North Pole and is treated as a land point. Other grids, for example, either tripolar or displaced pole grids, are not easily implemented within the Met Office Unified Model structure. Convergence of the meridians toward the North Pole on the spherical grid requires the tracers and baroclinic velocities to be Fourier filtered northward of 80°N to maintain stability. No filtering is necessary in the Southern Hemisphere. Fourier filtering undoubtedly has some impact, although the simulation is not obviously degraded within the filtering zone.

The ocean model has 40 unevenly spaced levels in the vertical with enhanced resolution near the surface to better resolve the mixed layer and atmosphere–ocean interaction processes. The level thicknesses are derived from an analytic expression to give near-10-m resolution close to the surface, increasing smoothly to near 300 m at depth. The use of an analytic function to derive the model levels results in the second-order accurate vertical differencing (Marti et al. 1992). The maximum ocean depth is 5500 m.

The external mode is solved with a linear implicit free surface scheme (Dukowicz and Smith 1994). In the marginal seas (the Black Sea and Caspian Sea, and the Great Lakes, which are not connected to other basins), an adjustment is performed after each time step to maintain the average global free surface height, which conserves water globally. This has no impact on the dynamics because it is only gradients of free surface height that are important for a linear free surface.

Lateral mixing of tracers uses the isopycnal formulation of Griffies et al. (1998) with constant isopycnal diffusivity. The Gent and McWilliams (1990, hereafter GM) adiabatic mixing scheme, which was used in the lower-resolution HadGEM1, is not used in HiGEM1.2. Tests showed that its inclusion created low eddy variability and erosion of fronts. The higher horizontal resolution of HiGEM1.2 means that eddies are, at least partially, represented. The adiabatic biharmonic scheme of Roberts and Marshall (1998; biharmonic GM) is used to reduce noise in tracer fields, particularly at high latitudes. To represent enhanced mixing at the ocean surface, tracers at levels 1 and 2 are mixed horizontally using a biharmonic scheme. All of the biharmonic mixing schemes use constant coefficients scaled by $\cos^3$(latitude) for numerical reasons to deal with the convergence of meridians approaching the North Pole.

The vertical mixing of tracers uses a hybrid scheme. The diffusivity at all depths is set using the Richardson number parameterization subject to a minimum, depth-dependent background viscosity. A bulk mixed layer scheme is used to determine the tracer values in the mixed layer. The vertical mixing of momentum also uses a hybrid scheme with a similar Richardson number parameterization to that used for vertical tracer mixing, but subject to constant minimum background diffusivity. The near-surface mixing of momentum follows HadGEM1, where the viscosity is a quadratic function of depth, thus providing a representation of a turbulent Ekman layer (Johns et al. 2006). For both momentum and tracers, the diffusivity is enhanced immediately below the mixed layer base to reduce the large gradients that can occur in this region.

Tracers are advected using a pseudo-fourth-order scheme (Pacanowski and Griffies 1998), except at the bottommost level, which uses an upwind scheme to reduce tracer extrema. Momentum advection uses a second-order-centered difference scheme. Bottom friction is implemented using a quadratic semi-implicit scheme.

The equation of state (EOS) used in HiGEM1.2 is that given in McDougall et al. (2003). The United Nations Educational, Scientific and Cultural Organization (UNESCO) EOS (Gill 1982) was updated by Feistel and Hagen (1995) by including more recent data. However, this gives density as a function of pressure, salinity, and in situ temperature. McDougall et al. (2003) derived a 25-term fit in terms of pressure, salinity and potential temperature, more convenient as the model uses potential temperature. A reference density (required by the Boussinesq approximation) of $\rho_0 = 1.035$ g cm^{-3} is used. Convection is parameterized using the full convection algorithm of Rahmstorf (1993). Further details of the ocean physics parameterizations are given in the companion paper by D. P. Stevens et al. (2009, unpublished manuscript).

c. Sea ice component

The configuration of the sea ice component in HiGEM1.2 follows that used in HadGEM1 closely, with the exception of changes to the values of some parameters and the introduction of a sub-time-stepping scheme for the ice dynamics. The main features are summarized below and further details can be found in McLaren et al. (2006). It contains elements of the Community Ice Code (CICE) elastic–viscous–plastic (EVP) model (Hunke and Lipscomb 2004).

Rather than existing as a separate submodel, the major part of the sea ice component resides within the ocean model with a small part in the atmosphere model. The ocean part solves for the dynamics, mechanical redistribution (ridging), and some of the thermodynamics. The atmosphere part calculates the atmosphere–ice fluxes and the ice surface temperature using the atmosphere time step to allow representation of the diurnal cycle. These fields are then averaged and communicated to the ocean model on a coupling time step.

The ice pack is modeled as a five-category ice thickness distribution that evolves through advection, ridging, and thermodynamic growth or melt. The ice velocities are calculated by solving the ice momentum equation using the EVP model of Hunke and Dukowicz (1997). The rate of change of ice momentum is a balance between ice–air drag, ice–ocean drag, Coriolis force, and internal ice stresses. The stresses are calculated from a constitutive equation that relates the ice stresses to the strain rates using an EVP rheology. The ice velocities are used to advect each ice category and the open-water category using an upwind scheme. Following advection, the ridging scheme (Hunke and Lipscomb 2004) converts thin ice into thick ice and creates open water. This ensures that in regions of convergent flow the ice area cannot exceed the gridcell area. The thermodynamic growth–melt is represented using the zero-layer model of Semtner (1976), applied to each category. The zero-layer model implies that there is no heat storage within the ice. After the thermodynamic model has calculated the thickness growth rates the linear remapping scheme of Lipscomb (2001) is used to calculate the transfer of ice between categories.

The ice model parameters are the same as those used in HadGEM1, with the exception of those related to the EVP subcycle time step. The EVP model introduces an elastic component to the viscous–plastic (VP) rheology as a means to increase the efficiency of the ice stress calculation. The EVP calculation is subcycled with a time step that is $O(100)$ times smaller than the ocean time step. In the limit of a very small subcycle step the EVP solution converges to the VP solution. Taking many subcycle steps is computationally expensive, but if insufficient steps are taken elastic waves can remain in the solution, which leads to noisy ice velocities. The ocean time step in HadGEM1 is 1 h and the EVP subcycle step is 30 s. HiGEM1.2 has an ocean time step of 20 min and an EVP subcycle step of 10 s.

The presence of a land point at the North Pole on the ocean grid means that no thermodynamic processes can affect the ice concentration at this point. However, sea ice does exist at this point and its evolution is calculated by a scheme that advects ice over the pole using ice velocities from the row immediately to the south.

In some early runs there were problems with stability of the ice model close to the North Polar island. The ice velocities at the northernmost ocean row became large enough to violate the Courant–Friedrichs–Lewy (CFL) stability criterion because of the convergence of meridians. The resulting noisy ice concentration field meant that the ridging process was unable to converge in a reasonable number of steps, and the model crashed with negative ice concentrations. In the ocean the stability problems are solved by Fourier filtering the velocity and tracer fields. Filtering cannot be performed on the ice velocities because it changes the mask of icy–nonicy grid cells. A possible solution would be to reduce the ocean time step, which is undesirable because it reduces the speed of the whole model. An alternative solution, which has been implemented, is to sub–time step the ice dynamics and ridging calculations. The calculation of the ice velocities, the advection of

the individual categories, and the ridging calculation is performed twice, with a time step of half the ocean time step followed by the thermodynamic part of the calculation over a whole ocean time step.

d. Boundary conditions

1) BATHYMETRY

The bottom topography is derived from two datasets: the 1/12° General Bathymetric Chart of the Oceans (GEBCO) Digital Atlas (BODC 2003) and the 1/30° dataset of Smith and Sandwell (1997). Both datasets are interpolated to the model grid by taking the median of all depths within each 1/3° × 1/3° grid cell for those cells where more than 62.5% of the points are sea points. This was found to give the best representation of coastlines. The resulting depth fields were not smoothed. In some regions, particularly the deep ocean basins, there are significant differences between the two datasets. In these regions the model depth was taken as the mean of the GEBCO and Smith and Sandwell (1997) values. The model depths were converted to model levels, and isolated bays (grid cells unaffected by advection) and single gridcell holes were filled. The topography was then adjusted in the regions of key sills and narrow pathways using data from Thompson (1995).

The land–sea mask is based on the GEBCO dataset with some adjustment of the coastline to give as accurate a representation as possible, commensurate with the 1/3° degree horizontal resolution. The connection between the Mediterranean Sea and the Atlantic Ocean at the Strait of Gibraltar is unresolved by the model grid, which requires a width of two tracer cells, or approximately 74 km, to allow advective transport. The Strait of Gibraltar is 12 km wide, so rather than modifying the topography to widen the strait, the choice was made to close the strait with a land barrier. The Mediterranean outflow is parameterized using the same scheme as in HadGEM1, in which there is a constant volume flux of 0.5 Sv (1 Sv $\equiv 10^6$ m^3 s^{-1}) from the Atlantic into the Mediterranean Sea over the top 108 m, and an equal return volume flux into the Atlantic Ocean over the depth range of 790–1155 m. The volume flux is smaller than the observed flux of 0.7 Sv (Baringer and Price 1997). However, similar to other ''z''-level models, the downslope flow of the Mediterranean Water, and entrainment of the overlying North Atlantic Central Water, is not well represented, and the value of 0.5 Sv gave the best simulation of the Mediterranean Water tongue in the North Atlantic. The entrances to the Red Sea and Persian Gulf are sufficiently well resolved to be open to the Indian Ocean. The Black Sea, Caspian Sea, and Great Lakes are represented on the ocean grid but are not connected to other ocean basins. As described in section 2b, the mean free surface height in the marginal seas is adjusted every time step to maintain an average global free surface height, which conserves water globally.

2) LAND SURFACE CONDITIONS

The model requires input datasets (ancillary files) to provide information about surface boundary conditions, such as orography, and other climatological fields, such as vegetation cover, which the model does not predict. The starting point in creating the ancillary files is deriving the land fraction from the land–sea mask of the ocean model. The coastal tiling scheme in the model enables a more accurate representation of fluxes at land–sea boundaries by combining ocean and land surface fluxes in proportion to the fraction of land within the grid box.

The orography has been derived from the 1′ Global Land One-Kilometer Base Elevation (GLOBE) dataset, which provides an accurate representation of the mountains and their subgrid-scale characteristics. The orography is smoothed with a Raymond filter to remove grid-scale and subgrid-scale features that are poorly represented in the model (Webster et al. 2003).

The land surface scheme of HadGEM1 uses fractional tiling to represent subgrid-scale surface heterogeneity. Nine land surface types are used, which include five vegetation types (C3 and C4 grasses, shrub, and needle leaf and broadleaf trees), bare soil, urban, permanent ice, and open water. Seasonally varying vegetation fractions for the five vegetation types were derived from the International Geosphere–Biosphere Program (IGBP) dataset (Loveland et al. 2000). A new specification for the soil albedo based on the analysis of Moderate Resolution Imaging Spectroradiometer (MODIS) data has been implemented over the Sahara (Houldcroft et al. 2009). Previously, the distribution of soil albedo over the Sahara was too uniform and had unrealistically high values.

3) AEROSOL EMISSIONS AND GREENHOUSE GASES

The interactive aerosol scheme in HiGEM1.2 requires emissions data and oxidant fields to drive the sulfur, black carbon, and biomass burning modeling. The raw datasets on which these are based are the same as for HadGEM1 (Martin et al. 2006), but interpolated to the higher horizontal resolution required for HiGEM1.2 (the vertical resolution is the same). For the sulfur cycle, seasonal anthropogenic sulfur dioxide emissions representing present-day values are from Smith et al. (2004). Natural emissions of dimethylsulfide

(DMS) on land are from Spiro et al. (1992), and monthly mean seawater concentrations of DMS are from Kettle et al. (1999). Annual mean volcanic sulfur emissions representing constantly emitting sources are from Andres and Kasgnoc (1998). Monthly mean three-dimensional fields of oxidants (OH, H_2O_2, and HO_2) for the sulfur cycle are taken from the offline Met Office Global Three-Dimensional Lagrangian (STOCHEM) model (Collins et al. 1997). Annual mean black carbon (soot) and monthly mean biomass burning aerosol emissions are taken from T. Nozawa (2003, personal communication).

The model is forced with fixed present-day concentrations of trace greenhouse gases (the concentrations of CO_2, CH_4, and N_2O are 345 ppm, 1656 ppb, and 307 ppb, respectively). Ozone is a seasonally varying two-dimensional field (latitude–height) derived from the Science Policy Assessment and Research on Climate (SPARC) climatology for 1990 (Randel and Wu 1999).

e. Model optimization

HiGEM1.2 is computationally very demanding, and good optimization of the code was considered essential to enable a multidecadal simulation within a few months. The unoptimized code was found to spend nearly 60% of the time in interprocess communication in the conjugate gradient solver routine in the ocean code (the ocean code runs serially with the atmospheric code). Furthermore, the sea ice code was found to be poorly load balanced. Implementing a faster global sum in the conjugate gradient solver and better load balancing in the sea ice resulted in a 62% speed-up of the code. With these improvements, HiGEM1.2 can achieve its target performance of 1 yr of model simulation per day on 256 processors on the U.K. Research Council's HPCx (IBM p5–575 cluster) system.

f. Model initialization and integrations

The atmosphere initial conditions were created from a September European Centre for Medium-Range Weather Forecasts (ECMWF) analysis field, with land surface conditions set to values from the ancillary files. The ocean initial conditions were created using September potential temperatures and salinities interpolated from the 1/4° *World Ocean Atlas 2001* (*WOA 2001*; Conkright et al. 2002), with initial ocean currents at rest. The sea ice fields were interpolated from September HadGEM1 model fields.

To demonstrate the impact of increased resolution an equivalent lower-resolution control, HadGEM1.2, has also been developed. HadGEM1.2 is very similar to HadGEM1 (Johns et al. 2006) but implements most of the changes to the parameterizations that are in HiGEM1.2. HadGEM1.2 has the same horizontal and vertical grids in the atmosphere and ocean as HadGEM1 and also uses identical bathymetry and orography.

Differences in the ocean code between HadGEM1.2 and HiGEM1.2 mainly result from their different horizontal resolution. In HiGEM1.2 the entrances to the Red Sea and Persian Gulf are resolved by the model grid, but the coarser resolution of HadGEMl.2 requires that these are parameterized. The horizontal mixing coefficients are larger than in HiGEM1.2, commensurate with the coarser grid, and the time step is increased to 1 h. HadGEM1.2 uses the GM adiabatic mixing scheme with the coefficients determined from the Visbeck et al. (1997) scheme. Horizontal viscosity in HadGEM1 was a combination Laplacian with a constant coefficient and biharmonic with the coefficient scaled by $\cos^3$(latitude). Investigations at the Met Office Hadley Centre found improvements to the equatorial circulation by changing the constant Laplacian viscosity to an anisotropic scheme. This is the formulation used in HadGEM1.2. The Laplacian viscosity has a zonal coefficient given by $K_x = 750\ [1 - \cos\ (\text{latitude})]$ $\text{m}^2\ \text{s}^{-1}$ and a meridional value $K_y = K_x(\Delta x/\Delta y)$, where Δx and Δy are the zonal and meridional grid spacings. The only differences in the sea ice model are that HadGEMl.2 has an EVP subcycle time step of 30 s and does not use the dynamics sub-time-stepping scheme.

Both HiGEM1.2 and HadGEM1.2 were run for 70 yr from the same initial conditions. A slightly earlier version of HiGEM, HiGEM1.1, has also been run for 130 yr on the Earth Simulator in Japan. Many aspects of the model's performance are similar to those of HiGEM1.2, and more details on these simulations can be found in Roberts et al. (2009).

3. Evaluation of model performance

The evaluation of the high-resolution model simulations has involved the wide range of NERC expertise related to the various components of the climate system, and used recent developments in earth observation for several components of the system. In this paper the focus will be on the mean state of the global climate system and how resolution in the atmosphere and/or ocean improves the overall performance of the model. One of the major results from HiGEM1.2 has been the representation of finescale air–sea coupled processes, especially in the tropical Pacific, as well as significant improvements in the simulation of El Niño and its global effects. A basic description of these achievements will be provided in section 4, and more detailed aspects of these phenomena, and of weather and ocean variability in HiGEM will be presented in related papers

(Roberts et al. 2009; Shaffrey et al. 2009, unpublished manuscript; D. P. Stevens et al. 2009, unpublished manuscript).

a. Overall energy balance

Table 1 compares the annual, global mean energy balance of the HiGEM1.2 and HadGEM1.2 simulations with observational estimates. The models show similar characteristics compared with the observations. The net radiation in both cases is close to being balanced, but this is achieved by reflecting too little solar radiation back to space and emitting too much thermal radiation. These characteristics are enhanced in HiGEM1.2, which has slightly less cloud and sea ice than the HadGEM1.2, more solar absorption at the surface, and consequently higher surface temperatures. It was decided not to attempt to retune HiGEM1.2 to bring the net radiation into balance, because the radiation imbalance is not large and the initial emphasis is to examine the impact of the higher resolution on atmospheric and oceanic processes, rather than to perform long-range climate predictions.

The differences between HiGEM1.2 and HadGEM1.2 also influence the evolution of the radiation balance and surface temperatures, as the model spins up during the integrations (Fig. 1). Initially, both models cool in accordance with the negative net top-of-atmosphere (TOA) radiation. The net outgoing longwave radiation (OLR) falls and the net TOA radiation rapidly adjusts to being slightly positive in HiGEM1.2 and to near zero in HadGEM1.2. As a result of the positive net TOA flux, HiGEM1.2 gradually warms to reach a global mean surface temperature close to the initial condition, whereas HadGEM1.2 remains cold.

The evolution of the sea ice has an impact on the longer time-scale evolution of the global radiation balance. Over the first few decades there is a reduction in sea ice in HiGEM1.2 (Fig. 1f), mostly around the Antarctic (see section 3f). After year 30 some Antarctic sea ice reforms, which leads to a reduction in net surface solar and a small reduction in the net TOA. It is also worth noting that in both models the net TOA has a small but positive value into the climate system. As shown by Johns et al. (2006) in HadGEM1, this is stored as heat in the ocean subsurface. A similar evolution of subsurface ocean temperatures occurs in HiGEM1.2 and will be discussed in greater detail in D. P. Stevens et al. (2009, unpublished manuscript).

Figure 2 shows the geographical distributions of the reflected solar and outgoing thermal and net radiation at the top of the atmosphere from HiGEM1.2, and the differences from the HadGEM1.2 control. The fields are averaged over years 21–70. The choice of averaging period was based on the time taken for the initial spinup of the TOA to become small. Unless otherwise stated, subsequent figures showing the means of various model quantities are also based on 21–70-yr averages.

TABLE 1. Annual global means of radiation and energy budget quantities from observational estimates, and HiGEM1.2 and HadGEM1.2 control runs. The observed estimates are taken from Kiehl and Trenberth (1997) and Wild and Roeckner (2006), adjusted to produce consistency between the various components. Uncertainties in the top of the atmosphere fluxes are ± 5 W m^{-2}. There are larger uncertainties at the surface. For example, estimates of the net surface solar radiation vary from 142 to 168 W m^{-2}. Observed values of precipitation and $P - E$ are from Trenberth et al. (2007). Unless otherwise stated, all values are in W m^{-2}.

Parameter	Observed	HiGEM1.2	HadGEM1.2
Incoming solar (TOA)	342	341.39	341.39
Outgoing solar (TOA)	107	97.06	99.81
Absorbed solar (TOA)	235	244.33	241.57
Outgoing thermal (TOA)	235	243.66	241.33
Net radiation (TOA)	0 ± 5	0.67	0.25
Solar cloud radiative forcing (TOA)	−48	−43.37	−44.91
Thermal cloud radiative forcing	25	23.67	23.99
Net solar (surface)	154	172.20	169.91
Net thermal (surface)	−50	−61.93	−61.75
Net radiation (surface)	104	110.27	108.16
Sensible heat flux	25	18.74	18.49
Latent heat flux	79	89.89	88.36
Precipitation (mm day^{-1})	2.60	3.11	3.05
$P - E$ over land (mm day^{-1})	0.73	0.72	0.70
$P - E$ over ocean (mm day^{-1})	−0.30	−0.30	−0.28
Cloud cover (%)	60	52	53

The tendency for lower cloud amounts in HiGEM1.2 is apparent in the generally negative values in the reflected solar differences. Martin et al. (2006) show that the simulation of subtropical marine stratocumulus in the atmosphere-only version of HadGEMl is considerably better than that in the previous model, HadAM3. Figure 2 shows that this is also the case in the control integration of HiGEM1.2; note the maxima in the reflected solar radiation off the west coasts of the continents, particularly off North and South America.

The difference plot shows positive values close to these coasts and negative values farther west, indicating that the cloud in HiGEM1.2 is concentrated closer to the land than in HadGEM1.2. This brings the reflected

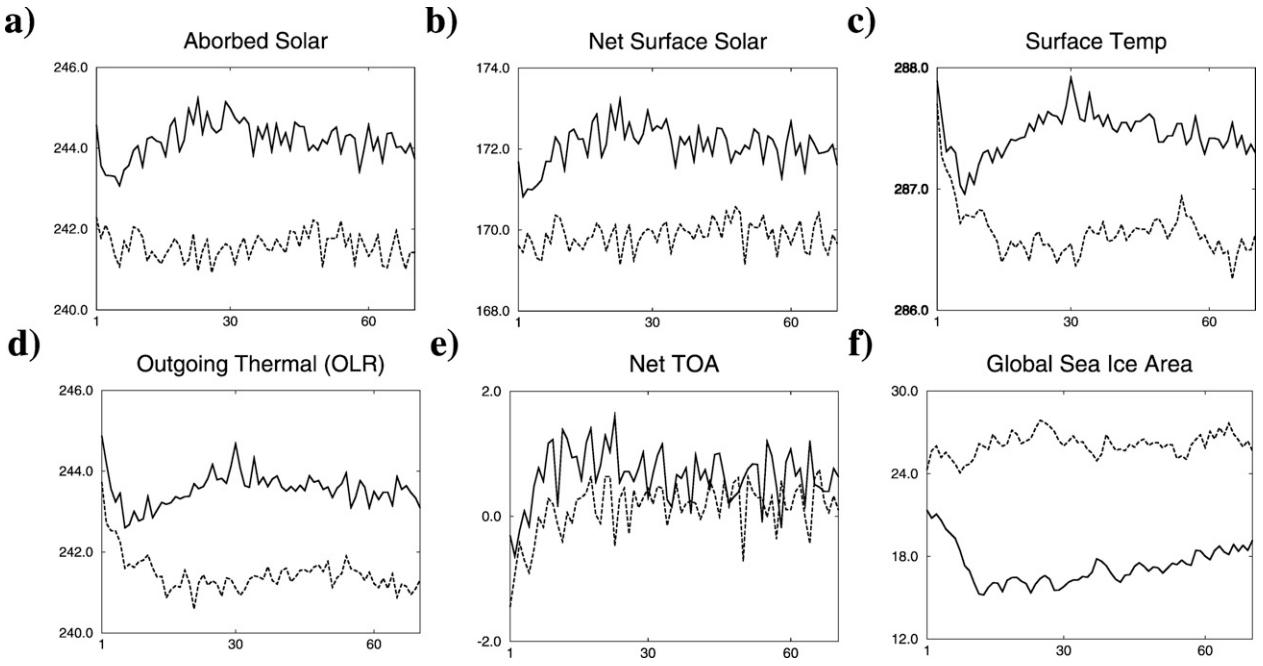

FIG. 1. Time series of global annual means for HiGEM1.2 (solid line) and HadGEM1.2 (dashed line) of (a) absorbed solar radiation (W m^{-2}), (b) net surface solar radiation (W m^{-2}), (c) global mean surface temperature (K), (d) TOA outgoing thermal radiation (W m^{-2}), (e) net TOA radiation (W m^{-2}), and (f) global sea ice area (10^{12} m^2).

solar radiation in HiGEM1.2 closer to observations over the subtropical stratocumulus decks. For example, averaged over the southeast Pacific (15°–25°S, 70°–80°W), the mean values of reflected solar radiation from HadGEM1.2, HiGEM1.2, and the 2001–05 Clouds and the Earth's Radiant Energy System (CERES) observations (Loeb et al. 2007) are 97, 112, and 127 W m^{-2}, respectively. Although the changes appear to be small, it is known that the simulation of sea surface temperatures in this region, and in the eastern tropical Pacific in general, is very sensitive to the cloud distribution (Ma et al. 1996).

There are also both positive and negative differences in the reflected solar and outgoing thermal fields over the tropical Indian and Pacific Oceans, resulting from systematic shifts in cloud cover. The large differences in both fields close to Antarctica are not due to cloud but to the smaller amounts of sea ice in HiGEM1.2. The effects of both the cloud and sea ice changes are readily apparent in the net flux differences, although the changes in the tropics disappear because of the tendency for the solar and thermal effects of clouds on top-of-atmosphere fluxes to cancel over regions of deep tropical convection. This cancellation was first observed by the Earth Radiation Budget Experiment (ERBE), and the fact that it occurs in the model is a further positive aspect of the simulations.

b. Surface climate

As already noted, globally HiGEM1.2 has slightly less cloud than HadGEM1.2 (see Table 1), which results in warmer surface temperatures. This can be seen in more detail in Fig. 3, which shows the annual mean sea surface temperature (SST) errors versus the *WOA 2001* (Conkright et al. 2002) climatology from both models and the difference between them. The warming of HiGEM1.2 relative to HadGEM1.2 means that the cold biases in the tropical and subtropical Pacific, Atlantic, and Indian Oceans in HadGEMl.2 are somewhat alleviated. In common with most coupled models (e.g., Solomon et al. 2007), there are warm biases in the upwelling zones off the Peruvian, Namibian, and Californian coasts, where the subtropical stratocumulus cloud decks are prevalent but are poorly captured by models. The warm bias is slightly weaker in HiGEM1.2 in association with increased cloud cover and better resolved coastal upwelling (Roberts et al. 2008).

Overall the east–west temperature gradient across the equatorial Pacific is better represented in HiGEM1.2, as is evident from the slight warming in the west and cooling in the east relative to HadGEM1.2 (Fig. 3e). This has important implications for the mean state of the coupled system; the excessively strong trade winds in HadGEM1.2 are reduced and the thermocline

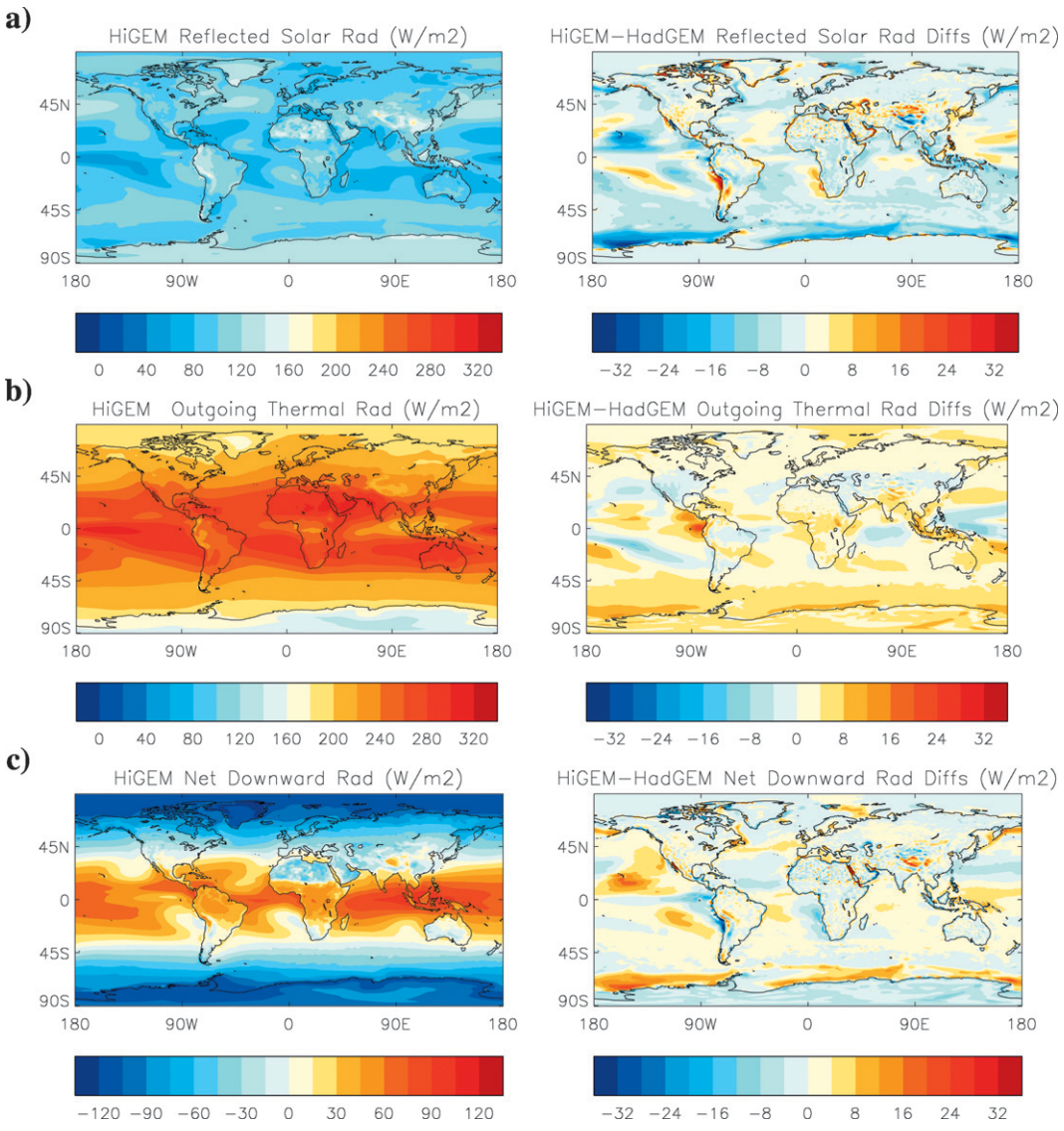

FIG. 2. Annual mean radiation budget (W m^{-2}) at the top of the atmosphere from (left) HiGEM1.2 and (right) the differences from the HadGEM1.2 for (a) reflected solar radiation, (b) outgoing thermal radiation, and (c) net downward radiation. The contour intervals have been matched to those in Fig. 13 of Martin et al. (2006), which also shows the ERBE observations.

is less steeply tilted. Both aspects have proved crucial for producing a significant improvement in El Niño and its global impacts (see section 4). The mean state of the tropical Pacific in HiGEM is described in more detail in Roberts et al. (2009).

The higher-resolution ocean model in HiGEM1.2 also allows a tightening of the SST gradients in the Gulf Stream, some improvements in the orientation of the Gulf Stream and North Atlantic Drift, and, consequently, a reduction in the temperature errors in the North Atlantic. This has a large impact on the wintertime cyclogenesis over the North Atlantic, discussed in more detail in Shaffrey et al. (2009, unpublished manuscript). Another difference between the models is the marked Southern Ocean warm bias in HiGEM1.2, which is associated with a reduction in Antarctic sea ice (see section 3f). This bias reduces in magnitude in the last few decades of the integration as the Antarctic sea ice partially recovers.

The annual mean sea surface salinity (SSS) errors versus *WOA 2001* (Conkright et al. 2002) are shown for both HiGEM1.2 and HadGEM1.2 in Fig. 3. The SSS errors in HiGEM1.2 are generally smaller than those in HadGEM1.2, which tends to be too fresh. However, the

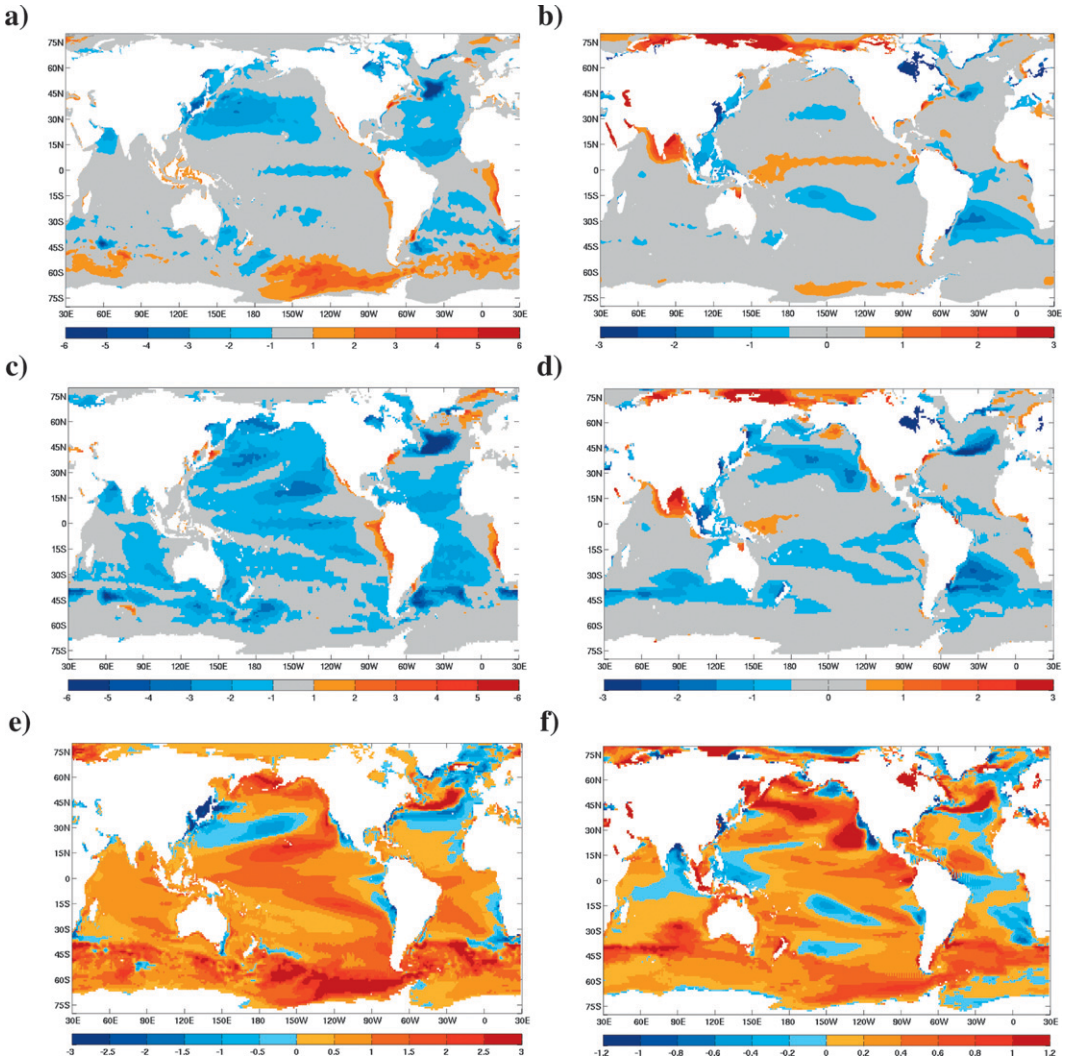

FIG. 3. The 21–70-yr annual mean HiGEM1.2 minus *WOA 2001* (Conkright et al. 2002) errors for (a) SST (K) and (b) SSS (PSU). (c), (d) Same as (a), (b), but for HadGEM1.2 minus *WOA 2001* (Conkright et al. 2002). HiGEM1.2 minus HadGEM1.2 differences for (e) SST and (f) SSS.

saline error in the tropical Pacific, which occurs in both models, is larger in HiGEM1.2. Both HadGEMl.2 and HiGEM1.2 are too saline in the Arabian Sea and the Bay of Bengal, associated with the lack of precipitation in the summer Indian monsoon in both HadGEM1.2 and HiGEM1.2 (see Fig. 6), a persistent feature of this family of Met Office Hadley Centre models (see Martin et al. 2006). The differences in SSS between the two models can be attributed in part to a slightly higher excess of evaporation over precipitation over the oceans in HiGEM1.2 (see Table 1), but may also be due to differences in upper-ocean mixing described in more detail in D. P. Stevens et al. (2009, unpublished manuscript).

The annual mean 1.5-m temperature errors over land for both HiGEM1.2 and HadGEM1.2 versus the Climatic Research Unit (CRU) land temperature climatology for 1961–90 (New et al. 2002) are shown in Fig. 4. Similar to the global mean surface temperatures and SSTs, the land surface of HiGEM1.2 is slightly warmer than HadGEM1.2, although both models are generally colder than the CRU dataset, especially over the Sahara, Saudi Arabia, and central Asia and at high latitudes over North America. The increased land surface temperatures in HiGEM1.2 improve some of the cold biases in HadGEM1.2, particularly over Australia, central and southern Africa, and South America. In a few places HiGEM1.2 is now warmer than the CRU dataset, for example, over the Indian subcontinent and the Guiana Highlands in South America, which may be associated with soil drying resulting from deficient

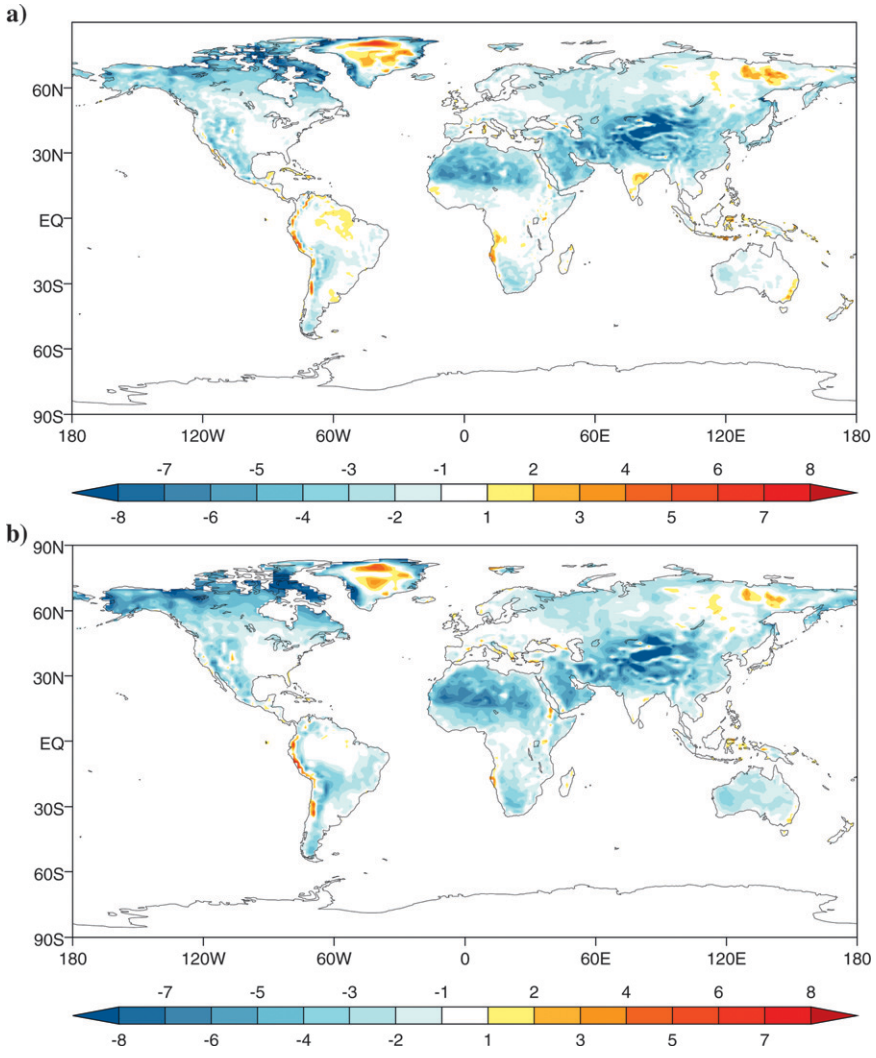

FIG. 4. Annual mean 1.5-m temperature errors (K): (a) HiGEM1.2 minus 1961–90 CRU 1.5-m temperature dataset and (b) HadGEM1.2 minus CRU 1.5-m temperatures.

rainfall (Fig. 6). Both models have deficient rainfall in these regions, so the temperature biases suggest that HiGEM1.2 has an overall more realistic land surface energy budget than HadGEM1.2. It is also worth noting that the cold temperature biases over the Sahara, West Africa, and Saudi Arabia are now substantially less than those in the original version of HadGEM1 used in IPCC AR4. This is primarily a result of including the MODIS-derived soil albedo over these regions, instead of the spatially homogenous values used in HadGEM1.

The annual mean precipitation distributions from HiGEM1.2 and from a 10-yr high spatial resolution climatology of merged Tropical Rainfall Measuring Mission (TRMM) satellite and rain gauge observations over the tropics (Huffman et al. 2007), are shown in Fig. 5. The improved representation of orographic forcing in HiGEM1.2 is evident in a comparison of the high-resolution observations and the modeled distributions of precipitation. The spatial patterns of precipitation in the vicinity of mountain ranges, such as the foothills of the Himalaya, the Ethiopian Highlands, or those on the islands of the Maritime Continent, are well captured in HiGEM1.2. Similarly, spatial patterns of precipitation are well captured over strong SST fronts such as the Gulf Stream and along coastlines facing the prevailing winds, for example, the eastern coastline of the Black Sea or the South Island of New Zealand.

However, it is clear in Fig. 5 that there are large-scale errors in the modeled distribution of precipitation. This can be seen more clearly in Fig. 6, which shows the annual mean errors for HiGEM1.2 and HadGEM1.2 versus the Climate Prediction Center (CPC) Merged

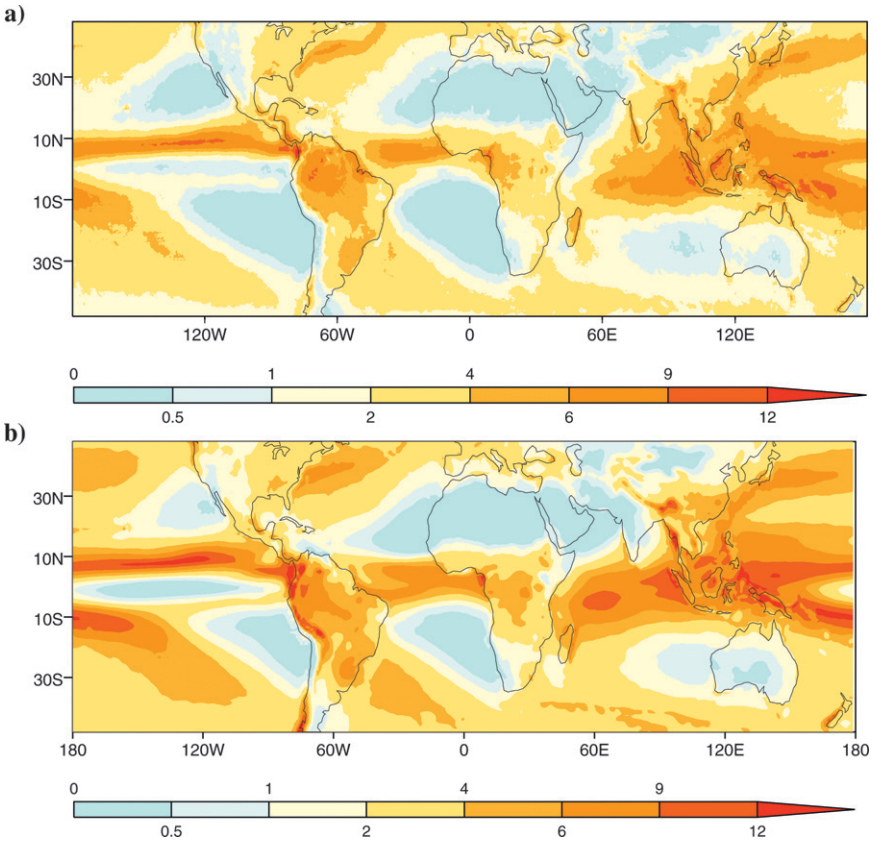

FIG. 5. The 21–70-yr annual mean precipitation (mm day^{-1}) from (a) the TRMM 3B43 10-yr climatology (Huffman et al. 2007) and (b) HiGEM1.2.

Analysis of Precipitation (CMAP) climatology (Xie and Arkin 1997). The CMAP climatology has a much lower spatial resolution than the TRMM merged precipitation dataset, but it is derived from a much longer period of observations (31 yr) and has global coverage. The global pattern of precipitation errors is generally unchanged with resolution, although the magnitudes of the errors are slightly reduced in HiGEM1.2 (a global rms error of 1.61 mm day^{-1} for HiGEM1.2 versus 1.63 mm day^{-1} for HadGEM1.2). There is a marked reduction in precipitation errors along the tropical Pacific ITCZ and over the tropical Indian Ocean, consistent with the pattern of SST errors shown in Fig. 3. Although the east–west SST gradient is improved in HiGEM1.2, it is still sufficiently in error that rainfall remains enhanced over the Maritime Continent. A recent study by Strachan (2007) has demonstrated that the pattern of precipitation errors in the Indian Ocean can be linked via an anomalous Walker circulation to those over the Maritime Continent, so it is not surprising that the tropical error pattern is largely unchanged in HiGEM1.2.

One of the most serious and persistent errors in all versions of HadGEM is the lack of summer monsoon rainfall over India. This is clearly evident in the annual mean error patterns and is not alleviated by the higher resolution and improved representation of orography in HiGEM1.2. As will be shown later, the low-level monsoon flow is, if anything, slightly too strong. Analysis of both integrations suggests that the lack of rainfall is not due to inadequate moisture supply, but to anomalous advection of dry air aloft, which acts to cap the convection. The lack of monsoon rainfall leads to strong summertime drying of the Indian land surface, which creates a further feedback on the monsoon precipitation.

Outside the tropics, however, HiGEM1.2 does show some improvements, especially over the North Atlantic, where the improved structure and orientation of the Gulf Stream and North Atlantic drift in HiGEM1.2 has led to changes in the storm track and the rain-bearing systems.

c. *Atmosphere*

Even though the increase in the horizontal resolution of HiGEM1.2 is less marked for the atmospheric component than it is for the ocean, it is nonetheless

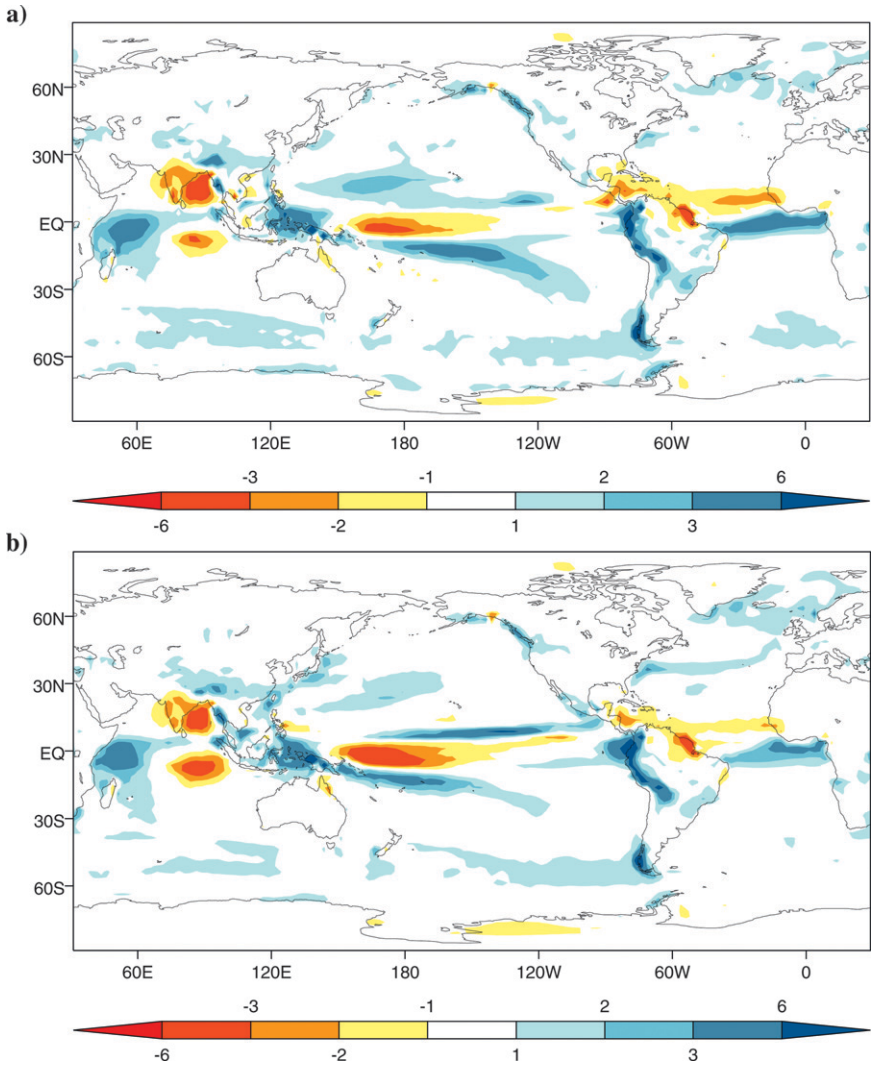

FIG. 6. The 21–70-yr annual mean precipitation errors (mm day^{-1}): (a) HiGEM1.2 minus CMAP and (b) HadGEM1.2 minus CMAP.

important to characterize and understand the changes in the atmosphere resulting from an increase in the resolution. A number of previous studies have investigated the sensitivity of different aspects of atmospheric models to horizontal resolution (e.g., Pope and Stratton 2002), but none of these studies have considered this in the context of a fully coupled ocean–atmosphere system where the SSTs can respond to the atmospheric scales of motion.

The differences between the atmospheric circulation in HadGEM1.2 and HiGEM1.2 are most pronounced during boreal winter. The differences at the surface can be seen in Fig. 7, which shows the December–February (DJF) mean sea level pressure errors against 40-yr ECMWF Re-Analysis (ERA-40) for HiGEM1.2 and HadGEM1.2. The mean sea level pressure errors in HiGEM1.2 have some similarities with those in HadGEM1.2, but mostly they are smaller in magnitude. There are some major errors in HadGEM1.2, and in earlier versions of HadGEM1 (Johns et al. 2006), which are largely eliminated in HiGEM1.2. The Aleutian low, which is very weak in HadGEM1.2, is better represented in HiGEM1.2, while the Icelandic low, which is too strong in HadGEM1.2, is largely corrected in HiGEM1.2. However, the high pressure error over the Azores remains, implying that the surface westerlies over the North Atlantic are still slightly too strong in HiGEM1.2. There are also some improvements in the mean sea level pressure errors over the Southern Oceans in HiGEM1.2, particularly to the east of the Drake Passage.

The improvements in the mean sea level pressure errors in HiGEM1.2, especially over the North Pacific,

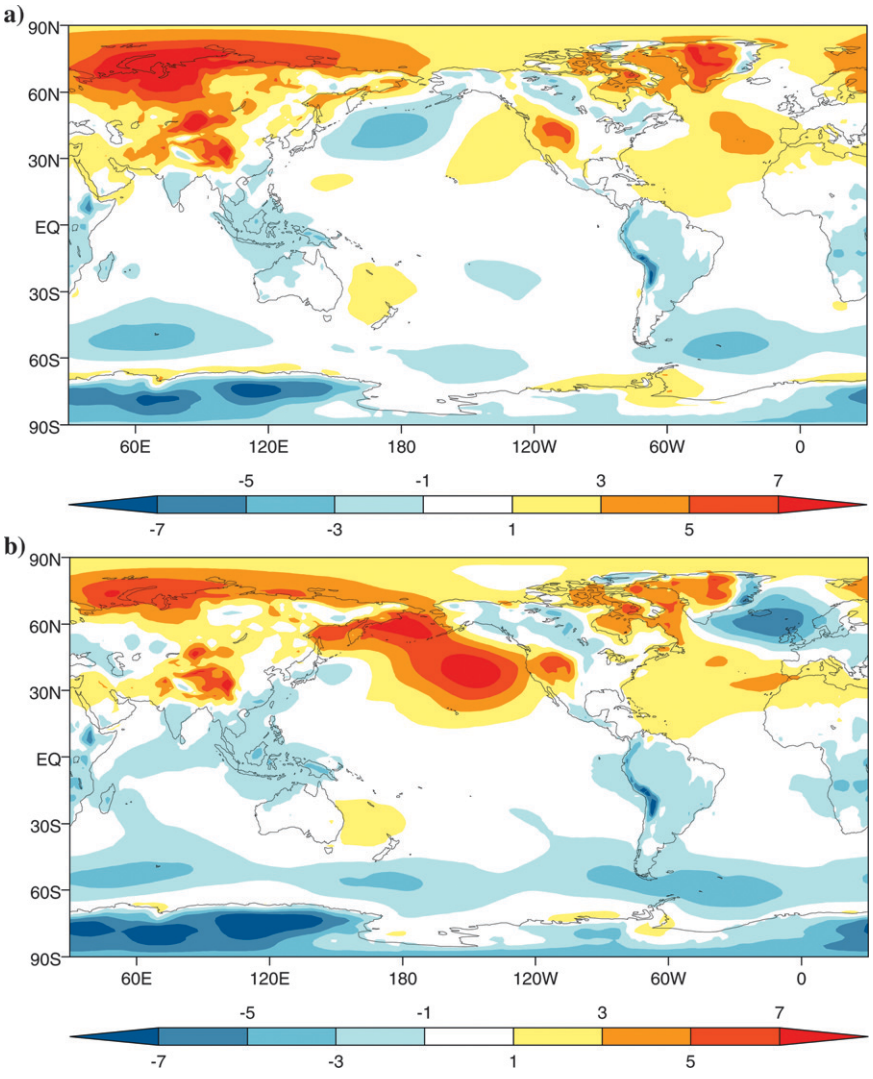

FIG. 7. The 21–70-yr DJF mean sea level pressure (hPa): (a) HiGEM1.2 minus ERA-40 and (b) HadGEM1.2 minus ERA-40.

can be interpreted in terms of a Rossby wave train emanating from the tropical Pacific. Figure 8a shows the difference in 500-hPa geopotential height between the two models, which clearly demonstrates a Pacific–North America (PNA)-type pattern with a succession of anticyclonic and cyclonic anomalies extending as far as the North Atlantic. The substantial improvement in the representation of the Aleutian low in HiGEM1.2 is clearly linked to this pattern.

There is good evidence to link this pattern of geopotential height anomalies with significant changes in tropical precipitation between the two models in boreal winter. Figure 8b shows the difference in DJF precipitation and 200-hPa divergence for HiGEM1.2 minus HadGEM1.2. The most noticeable changes in precipitation are over the northwest tropical Pacific, where there is a strong increase in precipitation over the seas surrounding the Philippines. Associated with the differences in tropical precipitation are changes in the upper-level divergent flow. Regions where the changes in the upper-level divergent flow impinge upon the gradient of absolute vorticity (e.g., near the flanks of the subtropical jet) will act as Rossby wave source regions (Sardeshmukh and Hoskins 1988). The region of anomalous upper-level divergence around the Philippines is one such Rossby wave source region, and the cyclonic response over the North Pacific is reminiscent of the Rossby wave response generated by anomalous heating in the tropics (Hoskins and Karoly 1981). It seems reasonable to argue, therefore, that the improvements in the Northern Hemisphere extratropical circulation during boreal winter in HiGEMl.2 can be

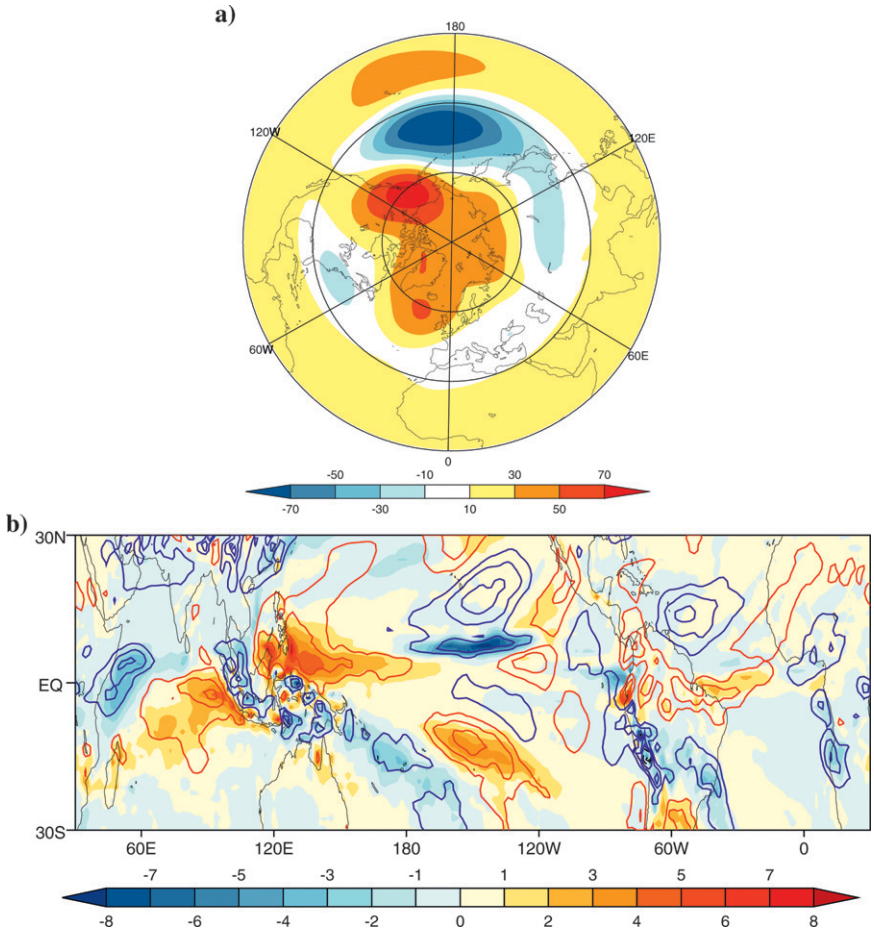

FIG. 8. (a) HiGEM1.2 minus HadGEM1.2 DJF 500-hPa geopotential height difference. The contour interval is 20 m. (b) HiGEM1.2 minus HadGEM1.2 DJF precipitation difference (colors) and 200-hPa divergence (contours) difference for years 21–70. The contour intervals are 1 mm day^{-1} and 10^{-6} s^{-1}. For divergence, red contours are positive and blue contours negative and the zero contour is not shown.

attributed to improvements in the SST patterns, and hence precipitation distributions over the Pacific warm pool.

On the other hand, the reduction of precipitation in the tropical Pacific ITCZ evident in Fig. 6, appears to be associated with a weakening of the North Pacific trade winds, which in turn may be related to a slight weakening of the North Pacific high in HiGEM1.2. This suggests that the reduction in precipitation in the tropical Pacific ITCZ is a response to changes in the circulation induced by the increase in precipitation around the Philippines. The improvement in the representation of the Icelandic low in HiGEM1.2 might also be interpreted as part of the Rossby wave response emitted from the tropical Pacific. However, there are also significant anomalies of precipitation in the tropical Atlantic that might force a remote response over the North Atlantic (e.g., Sutton et al. 2001) and also changes in the North Atlantic SST, which have an impact locally on the atmosphere (e.g., Kushnir et al. 2002).

The improvement in boreal wintertime circulation in HiGEMl.2 is further demonstrated in the 200-hPa zonal wind shown in Fig. 9. The location of the subtropical jet over the North Pacific is substantially improved, as expected from the stationary Rossby wave pattern shown in Fig. 8. The strength and orientation of the subtropical jet is also improved over the North Atlantic.

In terms of the boreal summer climate, the impact of higher resolution is less evident. Figure 10 shows the June–August (JJA) errors in the 850-hPa wind field in HiGEM1.2 and HadGEM1.2 versus ERA-40. Both models have an overly intense South Asian monsoon flow, despite the lack of rainfall over the Indian subcontinent. This westerly bias is more pronounced in HiGEM1.2 and extends farther into the northwest Pacific. On the other hand, HiGEM1.2 shows a reduced

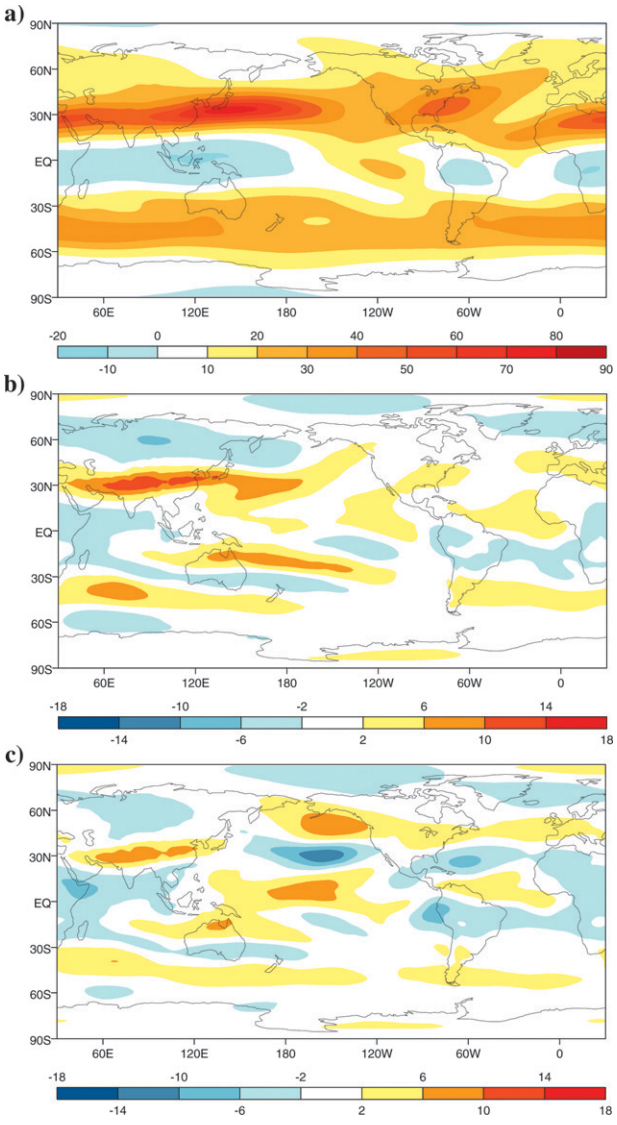

FIG. 9. The 21–70-yr DJF 200-hPa zonal winds (m s^{-1}) for (a) ERA-40 and wind differences, (b) HiGEM1.2 minus ERA-40, and (c) HadGEM1.2 minus ERA-40.

bias in the equatorial easterly Pacific trades, associated with the improvements in the east–west SST gradient. Over the southern oceans the notable feature is the reduction of the cyclonic anomaly to the west of South America in HiGEM1.2, which can be interpreted as a Rossby wave response to the improved heating pattern over the Indo-Pacific warm pool in the same manner that the NH wintertime circulation was improved.

Overall, the impacts of higher resolution on the mean circulation in the atmosphere are felt mostly through the remote effects of the improved heating patterns over the Indo-Pacific warm pool. There are more subtle adjustments in the subtropical jets that can be linked to changes in storm-track activity, which will be described in more detail in Shaffrey et al. (2009, unpublished manuscript).

d. Aerosols

The interactive aerosol scheme in HiGEM1.2 is the same as for HadGEM1, described in Martin et al. (2006). No changes were made to the parameterizations in the aerosol schemes to allow for the increased horizontal resolution in HiGEM1.2, and differences in total global burdens were found to be small (<6%; see Table 2), indicating that the schemes are robust in this respect. However, there are some regional differences in the aerosol distributions in HiGEM1.2 and HadGEM1.2, as can be seen in Fig. 11, which shows the annual mean column loadings of sulfate and biomass aerosols in HiGEM1.2 and differences from the HadGEM1.2 control. Some of the differences in aerosol loadings are associated with changes in circulation between HiGEM1.2 and HadGEM1.2. In particular, the increases in sulfate aerosol over the northwest Pacific may be related to increased advection from local sources over East and South Asia through intensification of the subtropical North Pacific jet (Fig. 9) and stronger monsoon westerlies (Fig. 10). Similarly, changes in biomass-burning aerosols over the north tropical Atlantic appear to be related to a southward shift and intensification of the African easterly jet (Fig. 10). However, the increase in sulfate aerosol around Antarctica in HiGEM1.2 is due to the reduction in sea ice relative to HadGEM1.2 (Fig. 17), allowing more dimethylsufhide to be emitted from the open sea surface.

Sulfate, black carbon, biomass-burning, and sea salt aerosols all feed back on the models via the direct radiative effect (scattering and/or absorption of radiation), and all but black carbon contribute to the first and second indirect effects [cloud albedo and precipitation efficiency; see Solomon et al. (2007, chapter 2)]. Figure 11 (bottom panel) shows the annual mean cloud droplet effective radius (r_e) from HiGEM1.2 and differences from the HadGEM1.2 control. In both models, r_e is calculated as a function of the cloud liquid water content and the aerosol concentration (Jones

TABLE 2. Global annual mean loadings of aerosol in HiGEM1.2 and HadGEM1.2

Aerosol type	HiGEM1.2	HadGEM1.2
S in Sulfate	0.52Tg	0.53Tg
Biomass	1.59Tg	1.51Tg
Black carbon	0.30Tg	0.31Tg

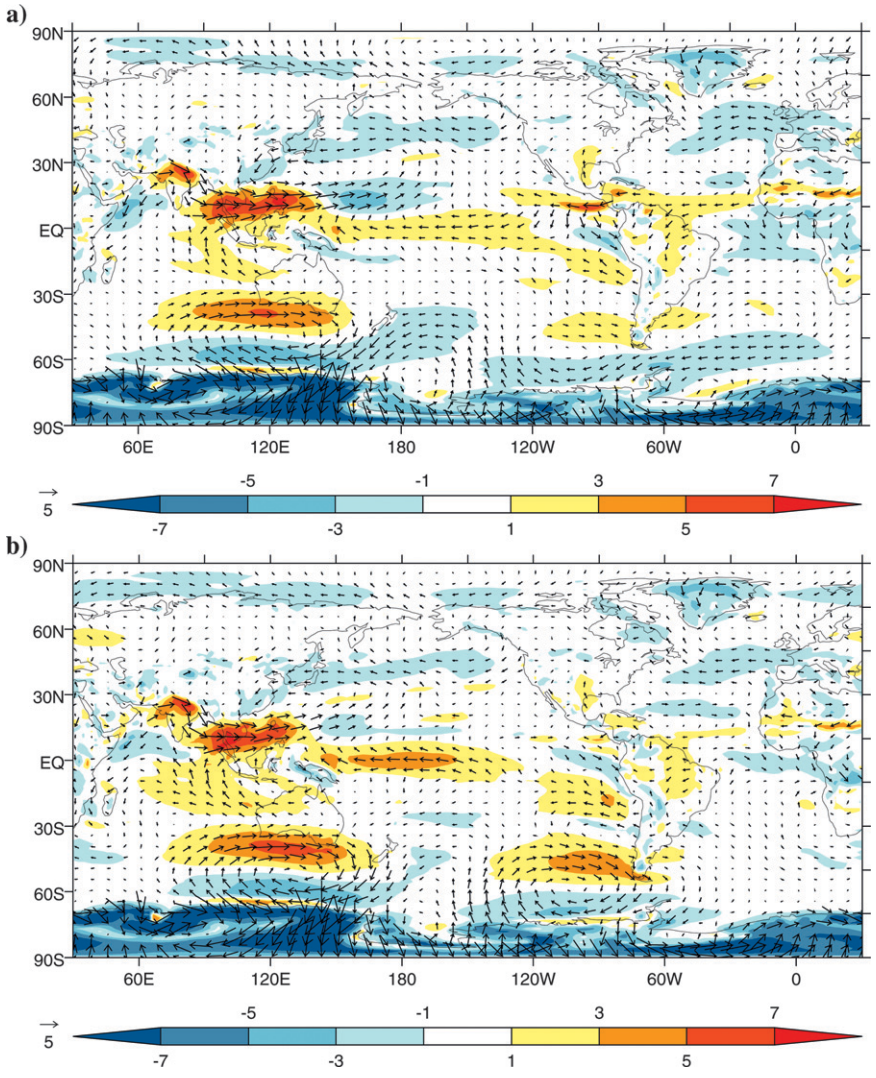

FIG. 10. The 21–70-yr JJA 850-hPa wind vector and wind speed differences (m s^{-1}) for (a) HiGEM1.2 minus ERA-40 and (b) HadGEM1.2 minus ERA-40.

et al. 2001). Martin et al. (2006, their Fig. 18) show that the simulated distributions from HadGEM1 compare reasonably well with the satellite retrievals from Han et al. (1994). Differences between HiGEM1.2 and HadGEM1.2 demonstrate a clear negative correlation between aerosol concentration and r_e, with more (less) polluted air giving rise to smaller (greater) values of r_e, for example, across the northern Pacific, off the east coast of Africa, and around Antarctica. In other regions, for example, off the west coasts of Africa and South America, it is the improved representation of marine stratocumulus cloud in HiGEM1.2 (noted above) that affects values of r_e, as seen from the positive correlation with the reflected solar radiation (see Fig. 2) in these areas.

An interactive dust scheme has not been included in this version of the model, but has been tested extensively in the atmosphere-only version, HiGAM1.2, where the increased atmospheric resolution and improved surface topography have yielded very good results, especially for Saharan dust (see M. J. Woodage et al. 2008, manuscript submitted to *J. Climate*).

e. Ocean

The increase in resolution for the ocean is more substantial than for the atmosphere, and a key question is whether the ability to permit the effects of eddies to be resolved more completely has a fundamental effect on the basic ocean circulation. Furthermore, the higher resolution allows a better representation of key aspects

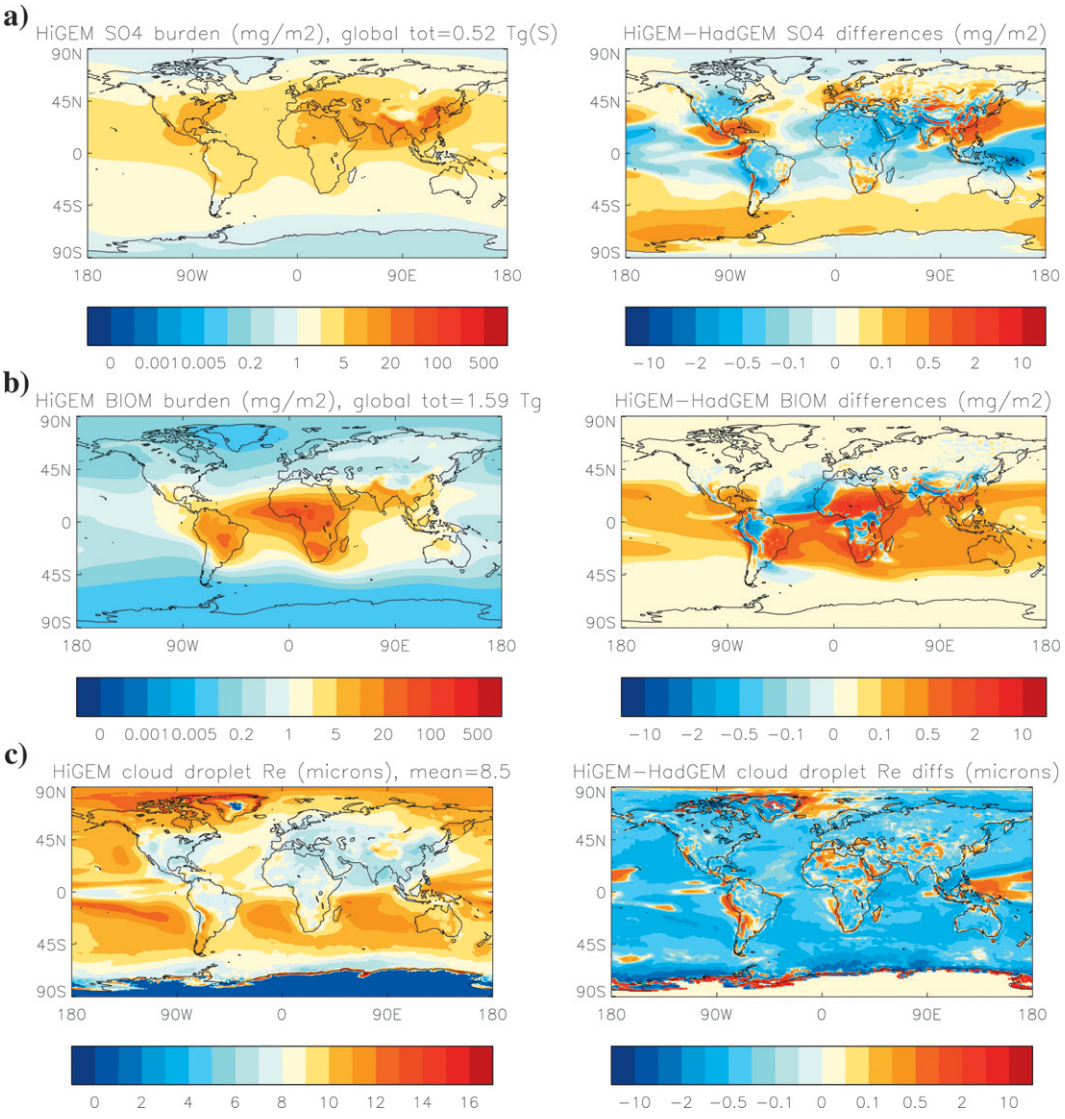

FIG. 11. Annual mean vertically integrated loadings (mg m^{-2}) from (left) HiGEM1.2 and (right) the differences from HadGEM1.2 of (a) sulfate and (b) biomass burning, while (c) the corresponding cloud droplet effective radii (μm) is shown.

of the bathymetry, including channels and sills. The transports through important straits and passages around the world's oceans are shown in Fig. 12. There is a general improvement in the transports through the straits linking the Arctic to the south (the Fram Strait, Denmark Strait, Iceland to Scotland Ridge system, and Bering Strait). In particular, the transport through the Fram Strait is much better represented in HiGEM1.2 than in the coarser-resolution HadGEM1.2.

The modeled transports through the Florida Strait are lower than observed. This is primarily due to the poor representation of transports through the narrow passages that link the North Atlantic and the Caribbean Sea, and eventually feed into the Florida Current. In HiGEM1.2 and HadGEM1.2 the flow through the Windward Passage is northward out of the Caribbean Sea, whereas the observed flow is 10.1 ± 2.4 Sv southward into the Caribbean Sea (Johns et al. 2002). The strength and direction of the transport through the Windward Passage has been shown to be sensitive to the frictional effects associated with the narrow passages into the Caribbean Sea (Wajsowicz 2002), but even at 1/10° horizontal resolution, Maltrud and McClean (2005) found that the Florida Strait transport was weaker than observed, because most of the transport passed out of the Caribbean Sea via the Windward Passage. The Indonesian Throughflow provides a important connection between the Pacific and Indian

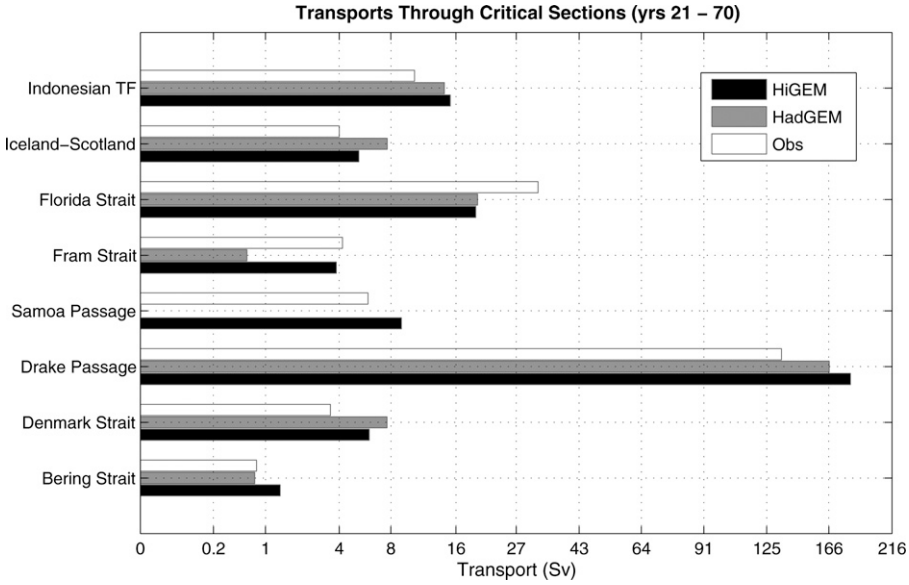

FIG. 12. Mean transports through critical sections of the world's oceans for HadGEM1.2 and HiGEM1.2. Observational values were obtained by Gordon (2001; Indonesian Through Flow), Hansen and Österhus (2000; Iceland-Scotland), Baringer and Larsen (2001; Florida Strait), Fahrbach et al. (2001, Fram Strait), Rundick (1997; Samoa Passage), Cunningham et al. (2003; Drake Passage), Macrander et al (2005) and (Jónsson and Briem 2003; Denmark Strait), and Woodgate et al. (2005; Bering Strait). Note the scaling on the x axis is not linear.

Oceans on both the local and large scale. Even at higher resolution, it is still not possible to resolve the complex topography of this region, and the transports in both models exceed the observed values by 3–4 Sv.

The strength of the Antarctic Circumpolar Current (ACC), as indicated by the transport through the Drake Passage, is 187 Sv for HiGEM1.2 and 169 Sv for HadGEM1.2. This is significantly higher than the 138 ± 13 Sv found from observations (e.g., Naveira Garabato et al. 2003), but well within the range of values found within the third Coupled Model Intercomparison Project (CMIP3) coupled climate models (Russell et al. 2006). In both models the wind stresses over the Southern Ocean are too strong, which contributes to the excessive ACC transport. In addition, the ACC transport in HiGEM1.2 is somewhat stronger than that found in HadGEM1.2. The stronger transport in HiGEM1.2 is partly due to open-ocean deep convective events in the Ross and Weddell Seas associated with the formation of persistent polynyas during the first few decades of the HiGEM1.2 integration (see section 3f). The deep convective events act to increase the meridional density gradient and coincide with an upturn in the ACC transport in HiGEM1.2 in the first few decades of the run. As the ice reforms later in the integration, the meridional density gradient decreases and the ACC transport in HiGEM1.2 reduces, albeit to a value that is still higher than observed [see D. P. Stevens (2009, unpublished manuscript) for more details].

Figure 13 shows the Atlantic overturning streamfunction for HiGEM1.2 and HadGEM1.2 overlaid with the zonal mean potential temperature differences from climatology (Conkright et al. 2002). Recent observational estimates from moored array instruments at 26°N, have been used to establish a relatively robust value for the Atlantic meridional overturning circulation of 18.7 Sv, with a standard deviations of 5.6 Sv (Cunningham et al. 2007), which compares favorably with both HadGEM1.2 (18.2 ± 3.0 Sv) and HiGEM1.2 (19.5 ± 2.8 Sv). The patterns of overturning streamfunction in both models are grossly similar, but there are a few minor differences. HiGEM1.2 has slightly weaker overturning than HadGEM1.2, and the overturning in HiGEM1.2 penetrates further into the subpolar North Atlantic. The overturning in both models is relatively deep for a z-level model, exceeding 3500 m in both models. Observational estimates at 26°N in the Atlantic suggest that below 3000 m there is a 7.8-Sv southward flow (Cunningham et al. 2007). This compares to the negligible southward flow below that depth seen in HadCM3 (Gordon et al. 2000) and the approximately 4-Sv southward flow in both HadGEM1.2 and HiGEM1.2. It is likely, however, that there may be further changes in the deep Atlantic water masses if the HiGEM1.2 and

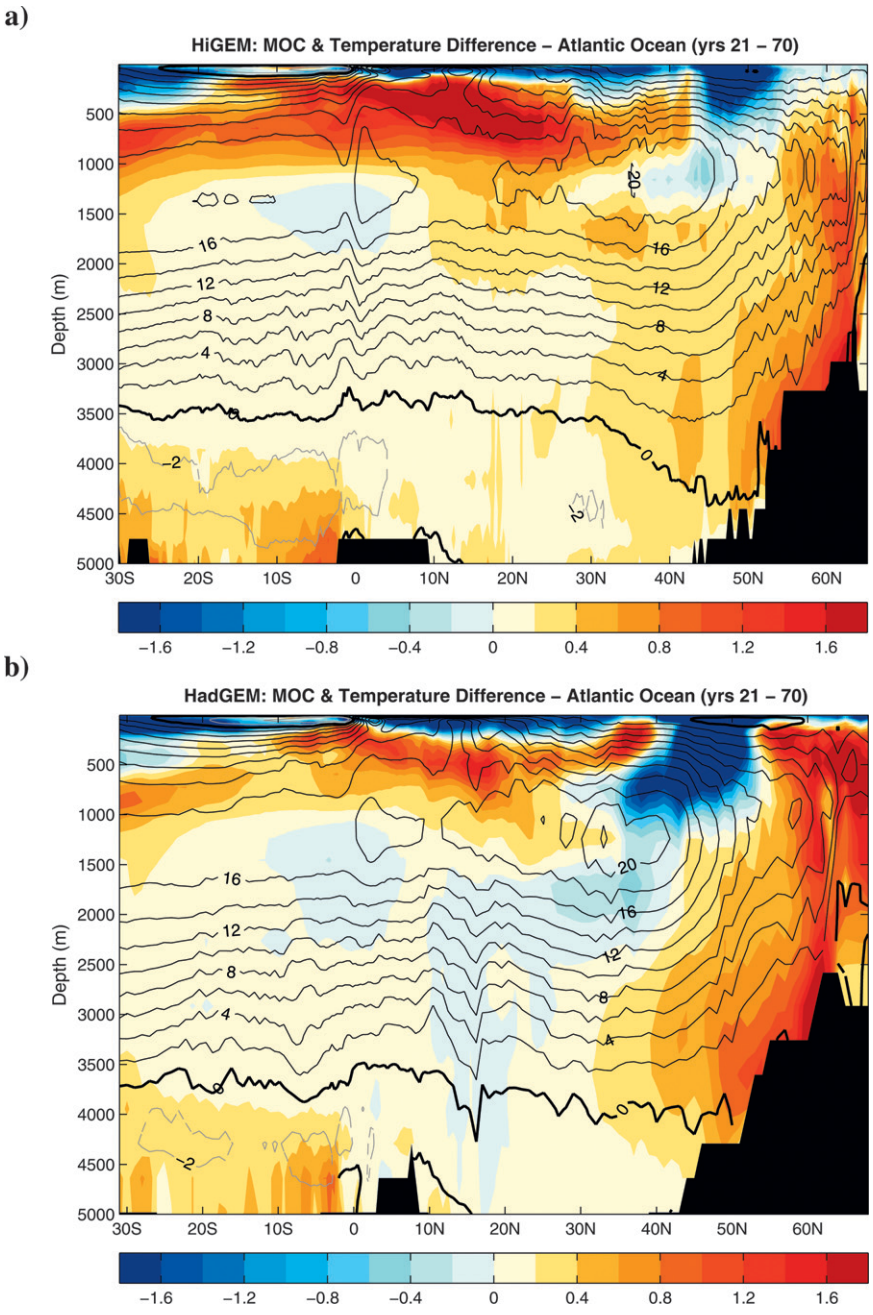

FIG. 13. Meridional overturning circulation (Sv) from the Atlantic Ocean (contours) and potential temperature difference (colors) from *WOA 2001* (Conkright et al. 2002) in (a) HiGEM1.2 and (b) HadGEM1.2.

HadGEM1.2 integrations described here were extended.

The temperature differences from climatology are shown in Fig. 13 (salinity errors are not shown but have a very similar spatial pattern). The high-latitude dense overflows in HadGEM1.2 are too warm and salty, more so than in the higher horizontal resolution HiGEM1.2 model. The z-level models have difficulty resolving the dense overflows in the northern North Atlantic (Beckmann and Doscher 1997), and coarser horizontal resolution will result in more spurious mixing in these sensitive regions. Figure 13 also shows the subsurface warming indicating a deeper thermocline, mentioned previously in section 3a, that develops in both HadGEM1.2 and HiGEM1.2 during the first few decades of the model integration.

Mesoscale eddy variability in the ocean is characterized by the sea surface height variability. To investigate how much variability is present in HiGEM1.2 and HadGEM1.2, the standard deviation in the model sea surface heights have been compared with satellite altimetry data (Fig. 14). The satellite variability field is calculated from 3 yr (1993–95) of 10-day fields of sea surface height anomaly data from the Ocean Topography Experiment (TOPEX)/Poseidon (AVISO 1996, 1998; Le Traon et al. 1998), gridded at a resolution of 1/4° and therefore comparable to the resolution of HiGEM1.2. The model variability field is calculated as the standard deviation of 5-day mean sea surface height fields over years 21–70.

The observations (Fig. 14a) show high levels of mesoscale eddy variability associated with the western boundary currents (e.g., the Gulf Stream, the Kuroshio, and the Agulhas) and along the Antarctic Circumpolar Current. Lower levels of variability are found in the eastern basins of the Pacific and Atlantic and in the tropics. HadGEM1.2, with its low resolution, does not explicitly permit eddies, except partially in the tropics where the resolution is increased in the meridional direction. The sea surface height variability (Fig. 14c) is much lower everywhere than observations. This is to be expected because the baroclinic instability processes that form eddies are not resolved.

Increasing the horizontal resolution to the eddy-permitting 1/3° scale of HiGEM1.2 has enhanced the eddy activity in the ocean, and in places resolved larger-scale eddy features (Fig. 14b). The maximum values found along the western boundary currents and along the path of the Antarctic Circumpolar Current are comparable with observations. However, in common with other eddy-permitting models (e.g., Maltrud and McClean 2005; Hallberg and Gnanadesikan 2006) there are a number of deficiencies. Regions of maximum variability tend to be spatially confined, because models of this resolution do not correctly propagate energy away from the high-energy source regions. The Gulf Stream separates from North America too far north with a persistent anticyclonic eddy. The eddies formed by the retroflection of the Agulhas Current follow too similar paths into the South Atlantic, as indicated by the narrow path of high variability. These deficiencies are known to be improved with further increases in resolution [Maltrud and McClean (2005); Ocean Circulation and Climate Advanced Modelling Project (OCCAM) 1/12°, online at http://www.soc.soton.ac.uk/JRD/OCCAM/]. However, as will be shown later, the presence of these eddies in HiGEM1.2, and hence variations in SST on the same scale, leads to features in the atmosphere that have important implications for the fully coupled system.

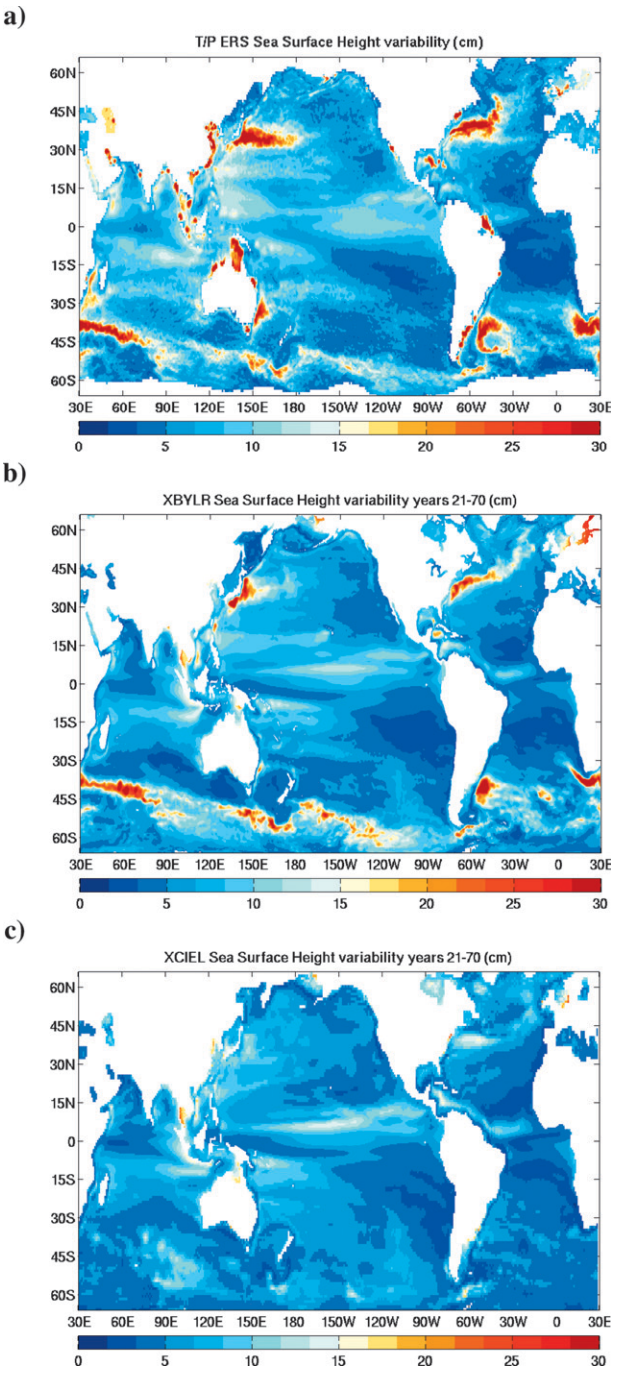

FIG. 14. Sea surface height variability (cm) from (a) TOPEX/Posiedon, (b) HiGEM1.2 (years 21–70), and (c) HadGEM1.2 (years 21–70).

The meridional heat transport by the oceans is a key factor in the accurate simulation of SSTs and indeed in the global energy cycle. The oceanic northward heat transports in HiGEM1.2 and HadGEM1.2 (Fig. 15) are broadly comparable with the direct estimates of Ganachaud and Wunsch (2003) and the National

Centers for Environmental Prediction (NCEP)-derived indirect estimates of Trenberth and Caron (2001). Note, however, that there is considerable uncertainty in the observational estimates. The global peak poleward heat transports produced by both models are weaker than the observations, though within the range of uncertainty. The peak northward heat transport is 1.13 PW for HiGEM1.2 and 1.26 PW for HadGEM1.2, compared with estimates of 1.18 PW by Trenberth and Caron (2001) and 1.27 PW by Ganachaud and Wunsch (2003). The lower value for HiGEM1.2 is consistent with its slightly weaker meridional overturning circulation (Fig. 13) and weaker overturning component of the heat transport. North of 40°N the northward heat transport is too large in both models for both the Atlantic and the global ocean. This is largely due to overly vigorous subpolar gyres, as evidenced by the large gyre component of the heat transport that dominates the northern North Atlantic (Fig. 15a). A partial explanation for the strong subpolar gyre transports may be the excessively strong westerly winds over the North Atlantic Ocean seen in both HadGEM1.2 and HiGEM1.2 (e.g., Fig. 7).

Both HadGEM1.2 and HiGEM1.2 exhibit a convergence of heat on to the equator resulting from eddy heat transport (actually all transient motions $\overline{v'T'}$) (Fig. 15b). This convergence is somewhat larger at higher resolution because tropical instability waves, which flux heat toward the equator, are better resolved by HiGEM1.2 (see section 4a). The larger convergence of heat is partially responsible for the improved simulation of equatorial SSTs seen at higher resolution, alleviating the cold SST errors in the equatorial Pacific (Roberts et al. 2009), which are common in climate models without flux adjustments (Guilyardi 2006).

The other region where the eddies play an important role in transporting heat is the Southern Ocean. Here the eddy component is negligible in HadGEM1.2, whereas it fluxes up to 0.5 PW poleward in HiGEM1.2. As can be seen in Fig. 14, eddy variability is negligible in the Southern Ocean for HadGEM1.2. The diffusive component in HadGEM1.2, however, includes the eddy parameterization of GM, which appears to provide a reasonable representation of the heat transport from the partially resolved eddies of HiGEM1.2.

Overall, the impact of increased resolution in the ocean component of HiGEM1.2 has been relatively small in terms of the overall global heat transport and mean overturning circulation. However, it is clear that the capability to represent ocean eddies and strong SST gradients in key regions, such as the eastern equatorial Pacific and the Gulf Stream, has a significant impact on the heat budget of the tropical Pacific (Roberts et al. 2009) and the North Atlantic. In turn this leads to important improvements in the mean climate of these regions, which has both global implications and substantial impacts on the regional weather and climate variability.

f. Sea ice

As noted in section 2D, the sea ice component in HadGEM1 is based around the CICE elastic–viscous–plastic model (Hunke and Lipscomb 2004), and a more detailed description of the sea ice model and comprehensive evaluation against observations is given in McClaren et al. (2006). The seasonal evolution and distribution of sea ice area and fraction in HiGEM1.2 and HadGEM1.2 is compared with those derived from satellite passive microwave observations using the bootstrap algorithm (Comiso 1999) for the Northern and Southern Hemispheres. Figures 16 and 17 show the distributions of sea ice fraction in the Northern and Southern Hemispheres for the months of March and September (i.e., the months of maximum/minimum extent) for HiGEM1.2, HadGEM1.2, and the observations. Overall there is greater sea ice area in HadGEM1.2 than in HiGEM1.2 in both hemispheres, which is consistent with the global mean surface temperatures being colder in HadGEM1.2.

The amplitude of the seasonal cycle of NH sea ice area (not shown) is larger than the observations in both models. The net result is that the magnitude of the sea ice area is well modeled in HiGEM1.2 in wintertime, but underestimated in summertime. On the other hand, consistent with the results of HadGEM1 (McClaren et al. 2006), the wintertime sea ice area is overestimated in HadGEM1.2 while the summertime modeled sea ice area is close to that observed. For all months in the Southern Hemisphere, the sea ice area is severely underestimated in HiGEM1.2, but overestimated in HadGEM1.2. The January–March (JFM) Arctic sea ice depths in HiGEM1.2 and HadGEM1.2 (not shown) look very similar to those for HadGEM1 shown in Fig. 12 of Johns et al. (2006), which indicate good agreement between the modeled and observed sea ice depths (Bourke and Garrett 1987).

In terms of the spatial distribution of sea ice fraction, the Northern Hemisphere fraction looks realistic in HiGEM1.2, but the sea ice melts back too far in September, particularly along the Russian coastline in the Arctic Sea. In HadGEM1.2 there is too much sea ice in March, particularly in the Labrador Sea, around the Bering Straits and in the Sea of Okhotsk. Even though the total September sea ice area in HadGEM1.2 is comparable with observations, Fig. 16 shows that there too much sea ice in the Labrador Sea and not enough in the central Arctic.

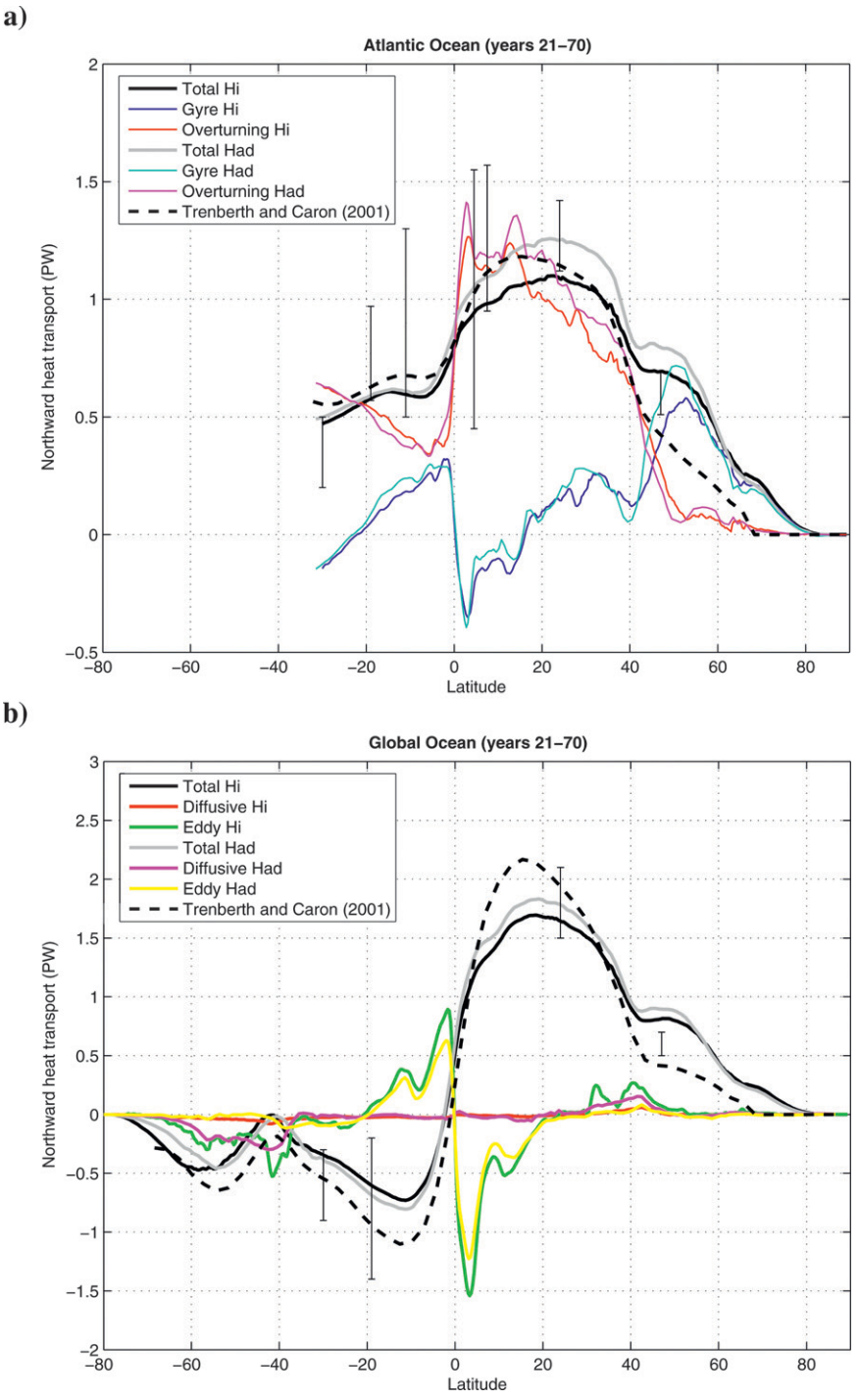

FIG. 15. Northward heat transport (PW; 1 PW = 10^{15} W) for (a) the Atlantic Ocean and (b) the global ocean. The total HiGEM1.2 transport is the solid black line, the total HadGEM1.2 transport is the solid gray line, and the NCEP-derived estimate of Trenberth and Caron (2001) is the dashed black line. Other components of the total transport are also shown. The error bars indicate the direct ocean estimates of Ganachaud and Wunsch (2003).

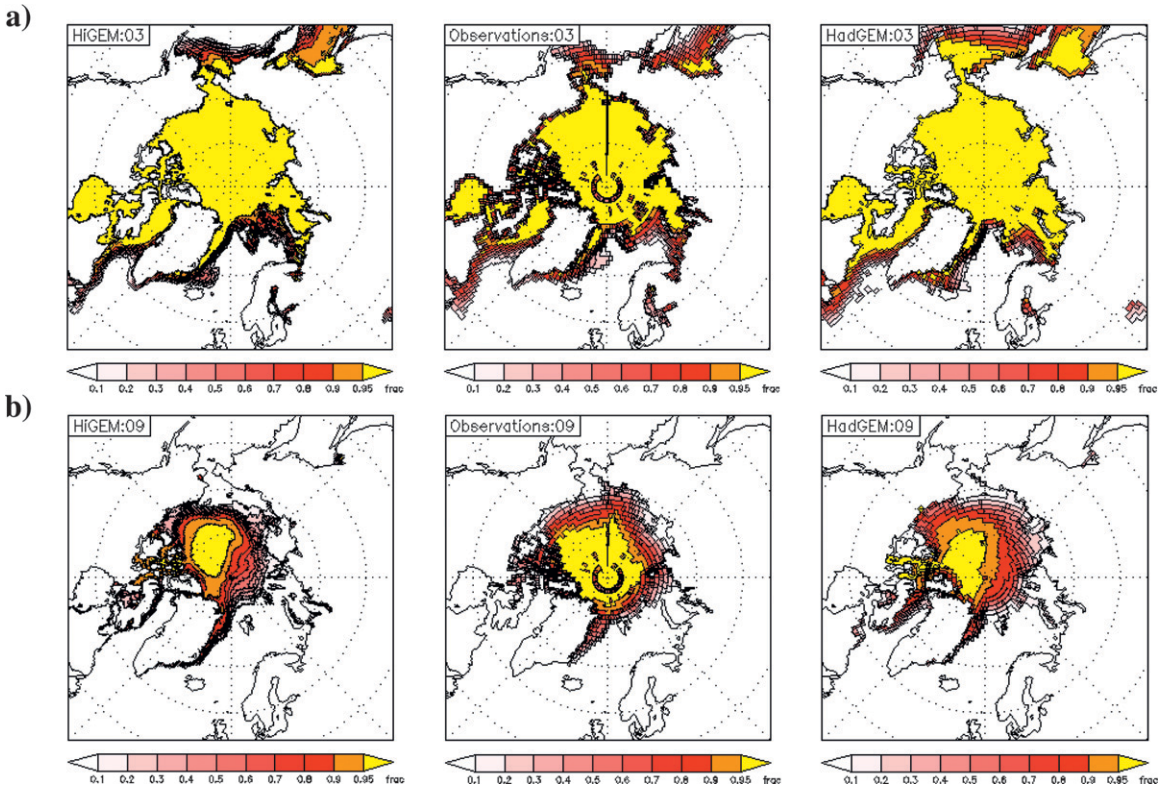

FIG. 16. The distribution of Northern Hemisphere sea ice fraction in (a) March and (b) September from (left) HiGEM1.2, (middle) observations (Comiso 1999), and (right) HadGEM1.2

For the Southern Hemisphere, although the total sea ice area in September in HadGEM1.2 is overestimated, the actual values of sea ice fraction are lower than the observed values over most of the Antarctic. In HiGEM1.2 the underestimation of Antarctic sea ice can be clearly seen by comparing the observed and modeled distributions of sea ice fraction (Fig. 17). The most striking feature of the September distribution of sea ice in HiGEM1.2 is the lack of ice in the Ross and eastern Weddell Seas, which, in individual years, appears as persistent open-ocean polynyas. These polynyas start to appear in year 8 of the run and, by year 14, much of the winter ice cover has disappeared from the Ross and Weddell Seas. The sea ice cover in the Weddell Sea starts to recover and, by year 21, a more realistic winter ice cover is reestablished. In the Ross Seas, however, sea ice fractions remain low, although they partially recover in the last few decades of the run (Fig. 1f).

Once the polynyas have appeared in the Weddell and Ross Seas, strong local feedbacks discourage the sea ice from reforming. In particular, an increased surface heat flux over the polynya region leads to increased ocean convection and entrainment of relatively warm and salty deep water into the upper ocean. The homogenization of the water column and the warming of the upper ocean by convection discourage sea ice formation, and the weak ocean stratification implies that an extensive heat loss from the polynya region is required before sea ice can reform. It is also possible that other local feedbacks such as sea ice import–export into the polynyas or the coupled ocean–atmosphere feedback described by Timmerman et al. (1999) might play a role in maintaining the open-ocean polynya in HiGEM1.2. Although open-ocean polynyas with multiannual persistence have been observed in the Weddell Sea (Gordon and Comiso 1988), it is unclear why they form so readily in HiGEM1.2. This issue will be dealt with in greater depth in a later paper.

The lack of Antarctic sea ice in HiGEM1.2 has a large impact both globally and locally on the model. The reduction in sea ice results in a reduction in surface albedo and an increase in net surface solar radiation, and thus a warming of the upper ocean of the Southern Hemisphere, particularly in Austral summertime. This can be seen, for example, in the difference in the SSTs between HiGEM1.2 and observations (Fig. 3). It is also worth pointing out that the underestimation of sea ice

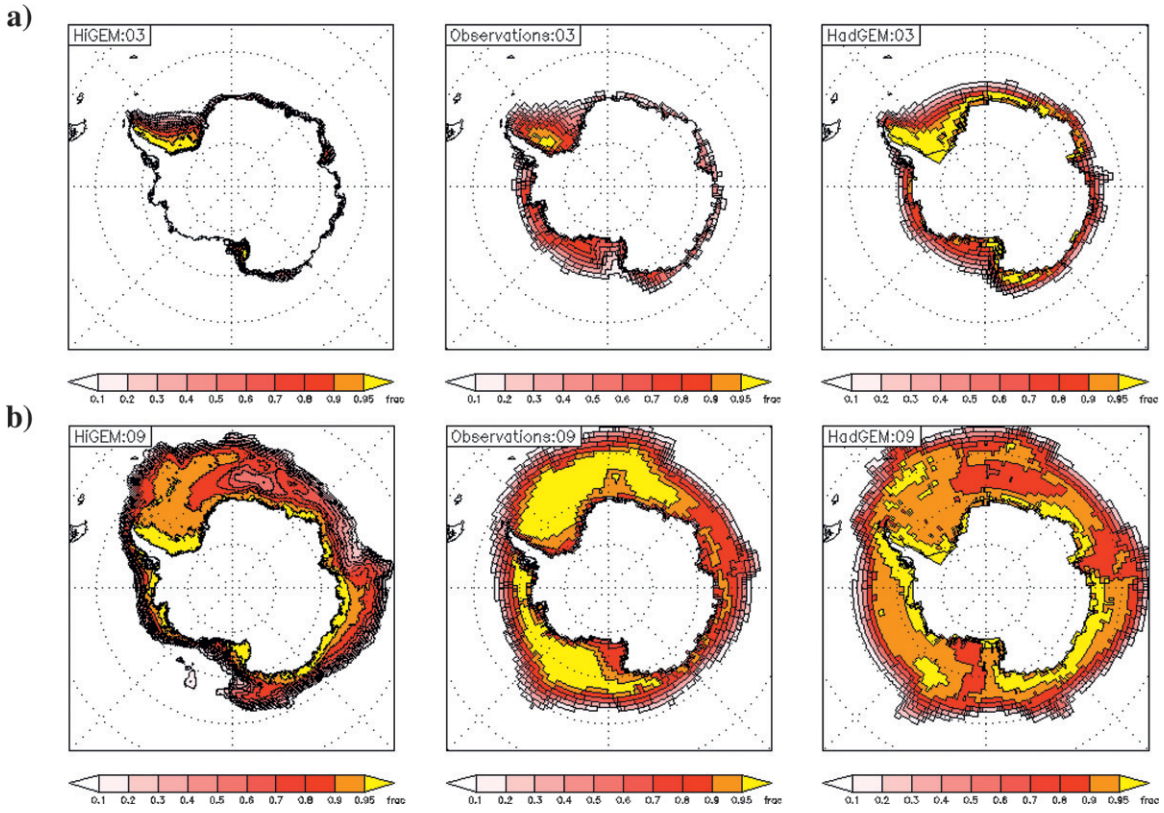

FIG. 17. As in Fig. 16, but for the Southern Hemisphere.

in HiGEM1.2 has a global impact on the model. As noted in section 3a the differences in Antarctic sea ice, along with the differences in total cloud amount, result in a reduction in the global albedo of HiGEM1.2 and contribute to the slight positive bias in the net TOA radiation (Table 1). The gradual reformation of sea ice around Antarctica during the run also leads to slow reduction in net surface solar and net TOA in the later part of the HiGEM1.2 integration.

Sea ice has proved to be the most challenging part of the development of HiGEM1.2, and although some aspects of the results show improvements in the simulation, the possibility for new feedbacks involving the formation of polynyas has raised a number of new and interesting research questions about the coupled behavior of the ocean–sea ice–atmosphere system and the potential for the coupled system to rapidly lose ice as a result of nonlinear feedbacks, which merit further investigation.

4. Atmosphere–ocean coupling

In the previous section the time mean state of the individual components of HiGEM1.2 were evaluated against HadGEM1.2 and observations. One interesting aspect of HiGEM1.2 is whether the local interactions that occur on smaller scales between the components have a significant impact upon the model. In particular, one important question that is raised is whether the smaller-scale features that can be resolved by the eddy-permitting ocean in HiGEM1.2 have an impact on the high-resolution atmosphere. This section describes a number of examples of where such small-scale ocean–atmosphere interactions are important.

a. Tropical instability waves

Because HiGEM1.2 has a high-resolution atmosphere coupled to a high-resolution ocean, it can simulate local, coupled air–sea interactions on relatively fine scales. One of the scales that is resolved by HiGEM1.2 is the interaction of tropical instability waves (TIWs) with the tropical atmosphere, an interaction that has been inferred from satellite observations of surface wind stresses for some time (Hashizume et al. 2001; Chelton et al. 2001). TIWs are mixed barotropic-baroclinic instabilities that form in the tropical countercurrent system. In the tropical east Pacific Ocean, TIWs

can be seen forming along SST gradients and strong shears flanking the cold tongue, and then traveling westward along the SST gradient.

TIWs are associated with substantial SST anomalies that can then have an impact on fluxes of moisture and heat into the atmosphere. The warming of the boundary layer, and the subsequent decrease in static stability associated with a warm SST anomaly, will act to increase the vertical mixing of momentum, so that warm SST anomalies will be associated with an increase in surface winds (Wallace et al. 1989). However, observations (Cronin et al. 2003) have also suggested that TIWs are associated with surface pressure anomalies; thus, a component of the surface wind response will be forced by pressure gradients (Linzden and Nigam 1987).

Oceanic TIWs have previously been resolved by ocean-only models and high-resolution ocean (but standard atmosphere resolution) coupled models (Roberts et al. 2004), and the impact of TIWs on the atmosphere has only been studied in high-resolution atmosphere-only integrations (Small et al. 2003). Coupled ocean–atmosphere models have not had sufficient resolution to resolve the small-scale coupled interaction between TIWs and the tropical atmosphere. Figure 18b shows instantaneous equatorial Pacific SSTs and wind stress divergence from HadGEM1.2. Some TIW activity is resolved along the tropical Pacific cold tongue in HadGEM1.2 where the meridional ocean resolution is enhanced, and where there are strong SST fronts, there is some indication of an atmospheric response. However, the low level of TIW activity in HadGEM1.2 contrasts with that found in HiGEM1.2 (Fig. 18a), which shows a series of TIWs along the northern, and to a lesser extent the southern, flanks of the cold tongue. The structure of the TIWs in HiGEM1.2 compares favorably with that seen from TMI SST satellite imagery (Chelton et al. 2001). The structure of the atmospheric response to the TIWs is also very similar to that seen in QuikSCAT imagery with regions of wind stress divergence seen along the crosswind SST fronts, suggesting that HiGEM1.2 is capable of simulating the coupled small-scale interactions between oceanic TIWs and the tropical atmosphere. The ability of HiGEM1.2 to capture the small-scale interactions between the TIWs and the atmosphere is described in much greater detail in Roberts et al. (2009).

There is good evidence to believe that the faithful representation of the TIWs and the associated atmospheric response in HiGEM1.2 are essential components of the marked improvement in the SSTs in the central and east equatorial Pacific, and hence in the east–west temperature gradient. As discussed in Roberts et al. (2009) the TIWs act to mix heat both zonally and meridionally in to the cold tongue region, thereby improving the local heat budget and the structure of the thermocline. Furthermore, the atmospheric response to the TIWs acts to break up the strong easterly trades in the model and potentially reduce the positive feedback between easterly wind stress, ocean upwelling, and cold SSTs.

One question raised by these results is how the interaction between TIWs and the atmosphere in HiGEM1.2 might be parameterized in a lower-resolution model such as HadGEM1.2. Developing such a parameterization would be difficult because it would need to be sufficiently complex to capture the nature of this coupled interaction, which emerges from being able to resolve motions in both ocean and atmosphere at the appropriate scale, and also realistically representing the small-scale nonlinear fluxes of heat, moisture, and momentum between components.

b. ENSO variability

One of the most important results of this study is the marked improvement in the simulation of El Niño and its global influence in HiGEM1.2. Figure 19 shows the monthly Niño-3 SST time series from the 70-yr integrations of HiGEM1.2 and HadGEM1.2. As described by Johns et al. (2006), and as evident in Fig. 20, El Niño events in HadGEM1.2 are smaller in magnitude and less coherent in structure than in the observations. This can be attributed to the excessively strong easterly wind stresses in the model that induce too much upwelling of cold water along the equatorial Pacific and confine the convective activity to the Maritime Continent. This means that the air–sea interaction and relaxation of the trades, which lie at the heart of El Niño, is inhibited in HadGEM1.2.

The corresponding 70-yr Niño-3 SST time series from HiGEM1.2 is shown in Fig. 19a. At the beginning of the integration there is a series of strong anomalies that indicate the model is adjusting in the tropical Pacific. Thereafter, there is much more interannual variability in HiGEM1.2 than in HadGEM1.2. This is also evident in the higher standard deviation of the monthly mean Niño-3 anomalies for HiGEM1.2 (0.89 K) versus HadGEM1.2 (0.76 K) and compared to the observed value of 0.84 K from HadISST (1955–2005). The power spectra from the HadGEM1.2 and HiGEM1.2 integrations are shown in Fig. 19c. Both models have a peak in power at periods between 3 and 6 yr, but there is more power in HiGEM1.2. This is broadly in line with the power spectra as calculated from a recent period of the HadISST SST observations (1955–2005).

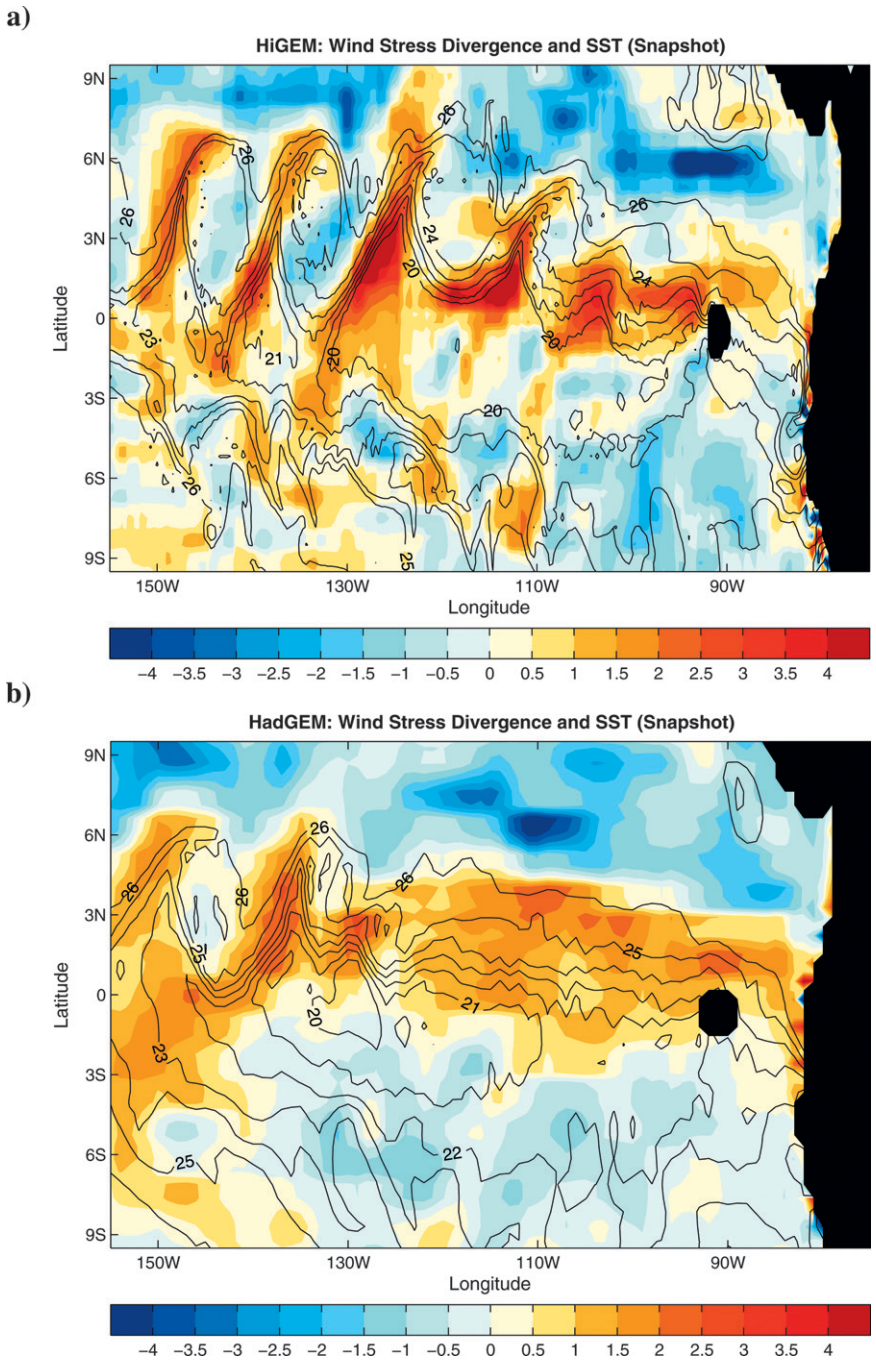

FIG. 18. Instantaneous fields of surface wind stress divergence (colors) and SST (contours) from (a) HiGEM1.2 and (b) and HadGEM1.2.

The difference in El Niño between HadGEM1.2 and HiGEM1.2 is further highlighted by composites of DJF SST and precipitation (Fig. 20) based on the eight largest El Niño events (after year 20), as measured by the DJF Niño-3 SST anomalies. Relative to HadGEM1.2, the representation of El Niño is substantially improved in HiGEM1.2. In comparison to observations, the DJF El Niño SST composite anomalies in HadGEM1.2 is weaker than observed, particularly in the east tropical Pacific, whereas the El Niño SSTs in HiGEM1.2 have a spatial pattern and amplitude that is much closer to that observed. However, El Niño SSTs still extend too far into the west tropical Pacific, which is a common failing of most climate models (Guilyardi et al. 2004).

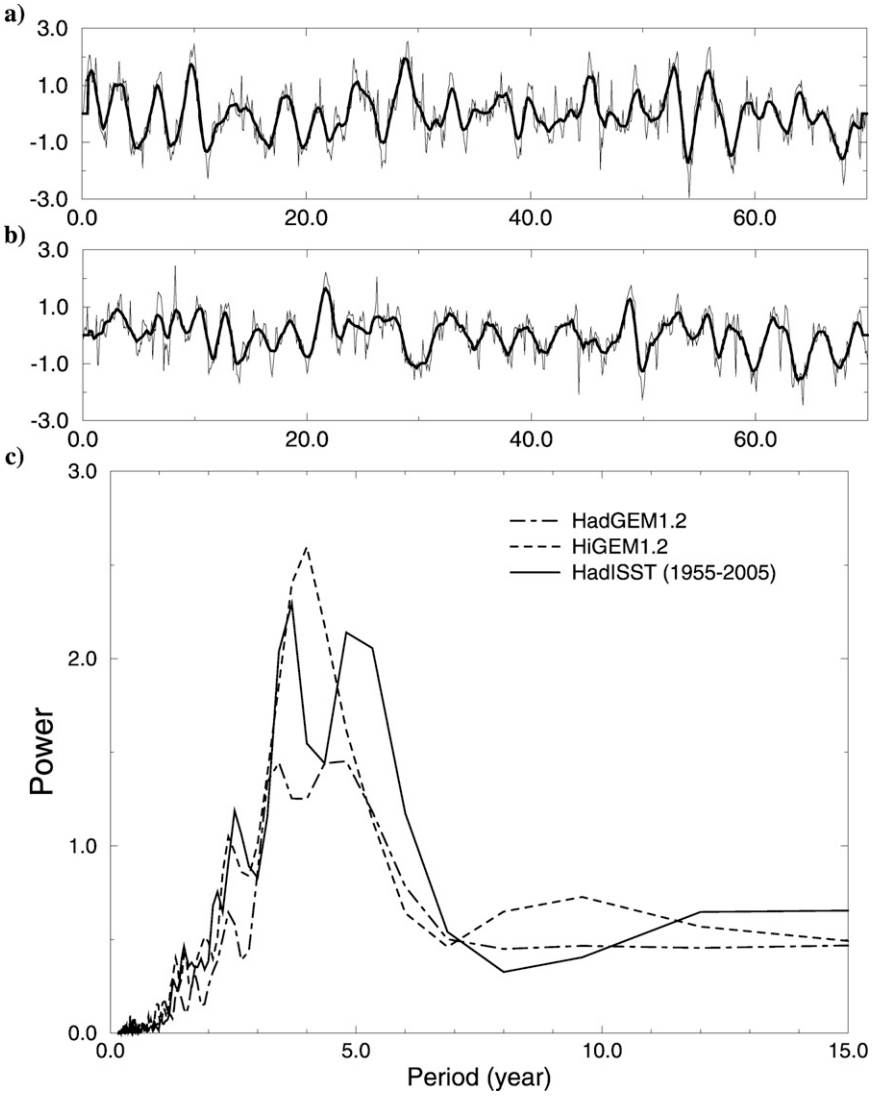

FIG. 19. The monthly (thin solid) and 12-month running mean (thick solid) time series of Niño-3 SSTs from (a) HiGEM1.2 and (b) HadGEM1.2. (c) The power spectrum of monthly mean anomalies of Niño-3 SSTs from years 21–70 of HiGEM1.2 (dashed) and HadGEM1.2 (dot–dashed) and from the HadISST observations for the period of 1955–2005 (solid).

The DJF precipitation composite anomalies for the models and observations (Figs. 20b,d,e) also indicate that the distribution of precipitation during an El Niño event in HiGEM1.2 is closer to observations than in HadGEM1.2. In HadGEM1.2 the precipitation over the west Pacific does not move as far eastward into the central Pacific as it does in the observations, because of the strong negative SST biases in that region. A similar bias occurs in HiGEM1.2, but to a lesser extent than in HadGEM1.2, and during an El Niño the precipitation moves farther into the central Pacific. In terms of tropics-wide teleconnections, it is notable that HiGEM1.2 is able to capture some aspects of the observed remote response of precipitation during an El Niño event, suggesting the model has some skill in replicating the observed transitions of the Walker circulation. For example, the excessive response over the Indian Ocean in HadGEM1.2 is much improved in HiGEM1.2.

The improvements in the precipitation response to El Niño in HiGEM1.2 translate into a significantly better simulation of the global ENSO teleconnections, with the exception of the Antarctic, where HadGEM1.2 is capable of capturing the observed teleconnections. Figure 21 shows the DJF composite mean sea level pressure anomalies from ERA-40 and both simulations. HiGEM1.2 has successfully captured the deepening of

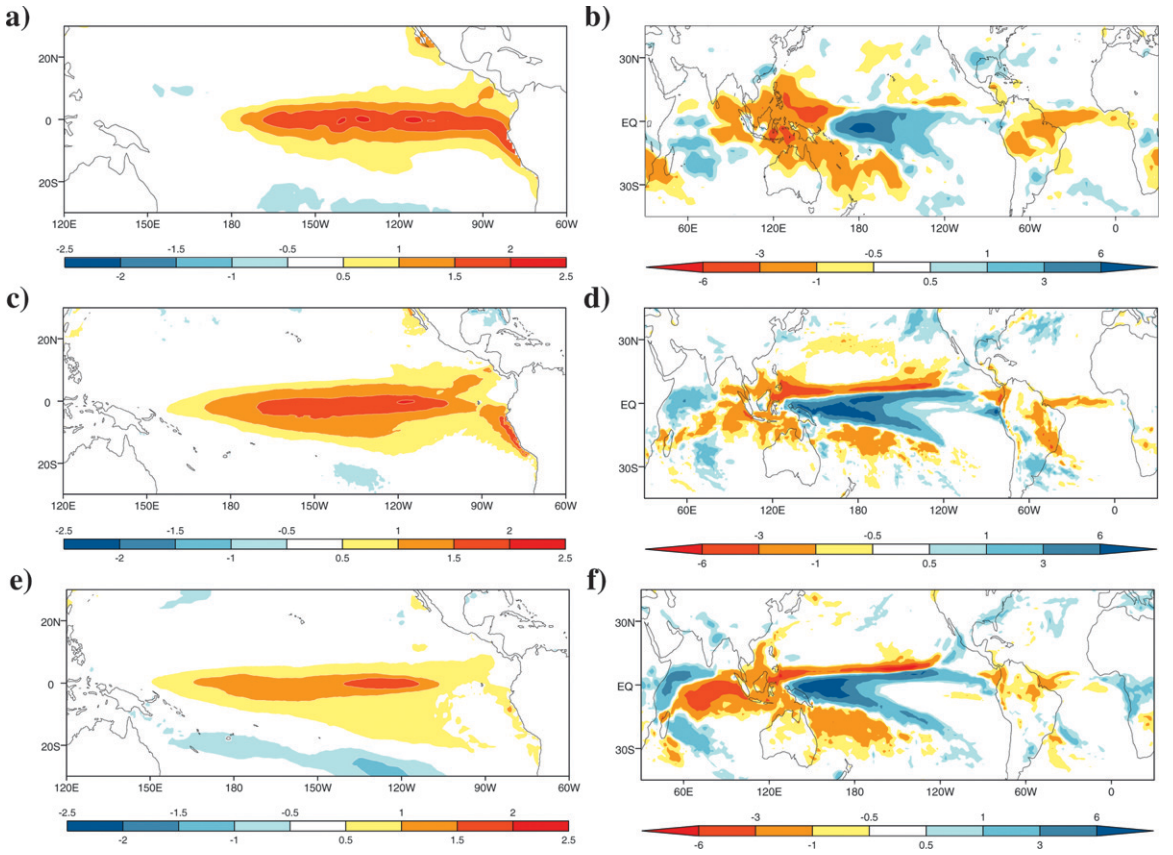

FIG. 20. El Niño DJF composite anomalies for SST (K) and precipitation (mm day^{-1}) from (a) the HadISST SST dataset and (b) the CMAP precipitation dataset and from (c),(d) HiGEM1.2 and (e),(f) HadGEM1.2.

the Aleutian low and the response over the Eurasian sector during El Niño events. However, the deepening of the Aleutian low in HiGEM1.2 occurs to the west of the observations, and the observed anticyclonic response over the Hudson Bay is displaced over the North Pole, which may be related to the rainfall not moving as far eastward into the central tropical Pacific (Spencer and Slingo 2002). The response in the Northern Hemisphere in HiGEM 1.2 is in stark contrast to that seen in HadGEM1.2, which fails to capture the observed extratropical teleconnections during an El Niño.

5. Concluding discussion

This paper describes the development and basic performance in a multidecadal simulation of the United Kingdom's new high-resolution global coupled model, HiGEM. More detailed analyses of specific aspects of the simulations will be presented in subsequent papers. Nevertheless, there are some important conclusions that can be drawn from this study.

Unlike most resolution studies, which have been largely based either on atmosphere-only or ocean-only models, or on increased resolution in one component only, in this study the resolution of both components has been increased simultaneously. This is an important point because a previous study by Roberts et al. (2004), in which only the ocean component was taken to higher resolution (1/3° as here), showed very little impact on the mean climate of the coupled model. One of the most striking results of this study is that when the atmosphere resolution is also increased, then the atmosphere is able to respond to the finescale detail in the SST field in a coherent way, with important implications for the mean climate and its variability. For example, it has been shown that tropical instability waves and the response to them of the near-surface winds, both now well resolved in HiGEM, have a significant effect on the mean state of the equatorial Pacific Ocean, and hence on the global mean climate and ENSO (Roberts et al. 2009).

The existence of coherent coupling between the ocean and atmosphere on fine spatial scales and on relatively short time scales challenges the conventional approach to climate modeling, which assumes that subgrid-scale processes can be parameterized within a

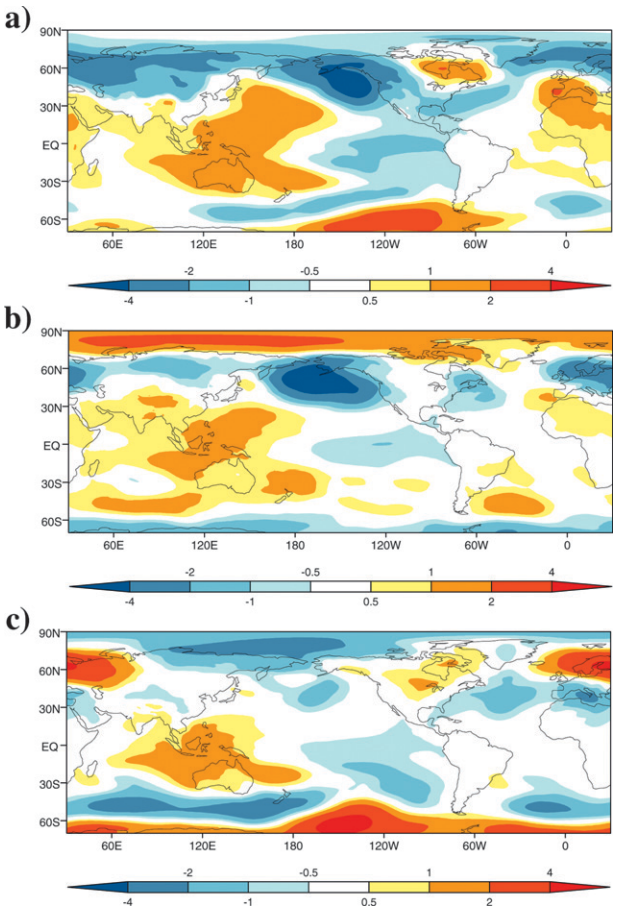

FIG. 21. El Niño DJF composite anomalies for mean sea level pressure (hPa) from (a) ERA-40, (b) HiGEM1.2, and (c) HadGEM1.2.

single component of the system. The results from HiGEM suggest that there may be important scales of *coupled* behavior that cannot be parameterized and that will therefore need to be resolved adequately. The implication of this is that there may be a minimum resolution for modeling the full behavior of the *coupled* system that may be higher than, or at least different from, that for the individual components. This also means it may be important for the atmosphere and ocean components of coupled models to have resolutions that are roughly equivalent, so that the atmosphere can respond to, and in turn force, the ocean on commensurate time and space scales.

The multiscale nature of the coupled processes demonstrated by HiGEM also has wider implications for the extension of physical climate models to full earth system models. As a demonstration of this point, Fig. 22 compares the annual mean surface wind stress curl and SSTs observed by QuikSCAT (Risien and Chelton 2008) and simulated by HiGEM1.2 and HadGEM1.2. The wind stress curl is important for forcing upwelling in the ocean, which is critical for biological production. In the QuikSCAT observations there is considerable structure in the wind stress curl along coasts, around islands, and in association with strong SST gradients (e.g., Gulf Stream) and large ocean eddy activity (e.g., Southern Oceans; see also Chelton et al. 2001, 2004). Many of these features are captured well by HiGEM1.2, but to a much lesser extent by HadGEM1.2, particularly those associated with islands and persistent small-scale SST structures (e.g., oceanic fronts). These deficiencies could be important when the model is coupled to ocean biology where the strength of upwelling regions is crucial for providing nutrients.

Figure 22 demonstrates again that the atmosphere in HiGEM1.2 is capable of responding to small-scale structures in the SST in a more realistic way, as has already been shown for tropical instability waves. Important features such as the Gulf Stream and the wind stress curl associated with it are better represented in HiGEM1.2. In particular, the Gulf Stream in HiGEM1.2 has tighter SST gradients and a more realistic orientation; in HadGEM1.2 the Gulf Stream is too zonal and the region of high SST gradients extends too far into the Atlantic Ocean.

Although HiGEM has demonstrated substantial benefits for some aspects of the climate system and its variability, some significant model problems remain, and some new ones have emerged. Errors in tropical rainfall patterns are particularly stubborn and are largely unaffected by increased horizontal resolution, apart from some improvements over the warm pool associated with a better simulation of the equatorial Pacific SSTs. It is becoming clear that current approaches to parameterizing tropical convection may be inadequate for representing the strong physical–dynamical coupling involved in the organized convection that forms the basis of tropical weather systems (e.g., Slingo et al. 2003). This organization occurs on scales that are much smaller than most global models can hope to represent at the current time. Thus, increasing resolution is not a panacea for all climate model errors, and much fundamental research on physical parameterizations, especially convection, remains to be done.

One of the most challenging aspects of developing HiGEM was the complexity of representing sea ice in a high-resolution coupled system. Considerable work was needed to reach a stable solution, and even then the model has produced unexpected nonlinear feedbacks that have resulted in a substantial loss of Antarctic sea ice, particularly in the Ross Sea. The formation of large and persistent polynyas in HiGEM led to a chain of

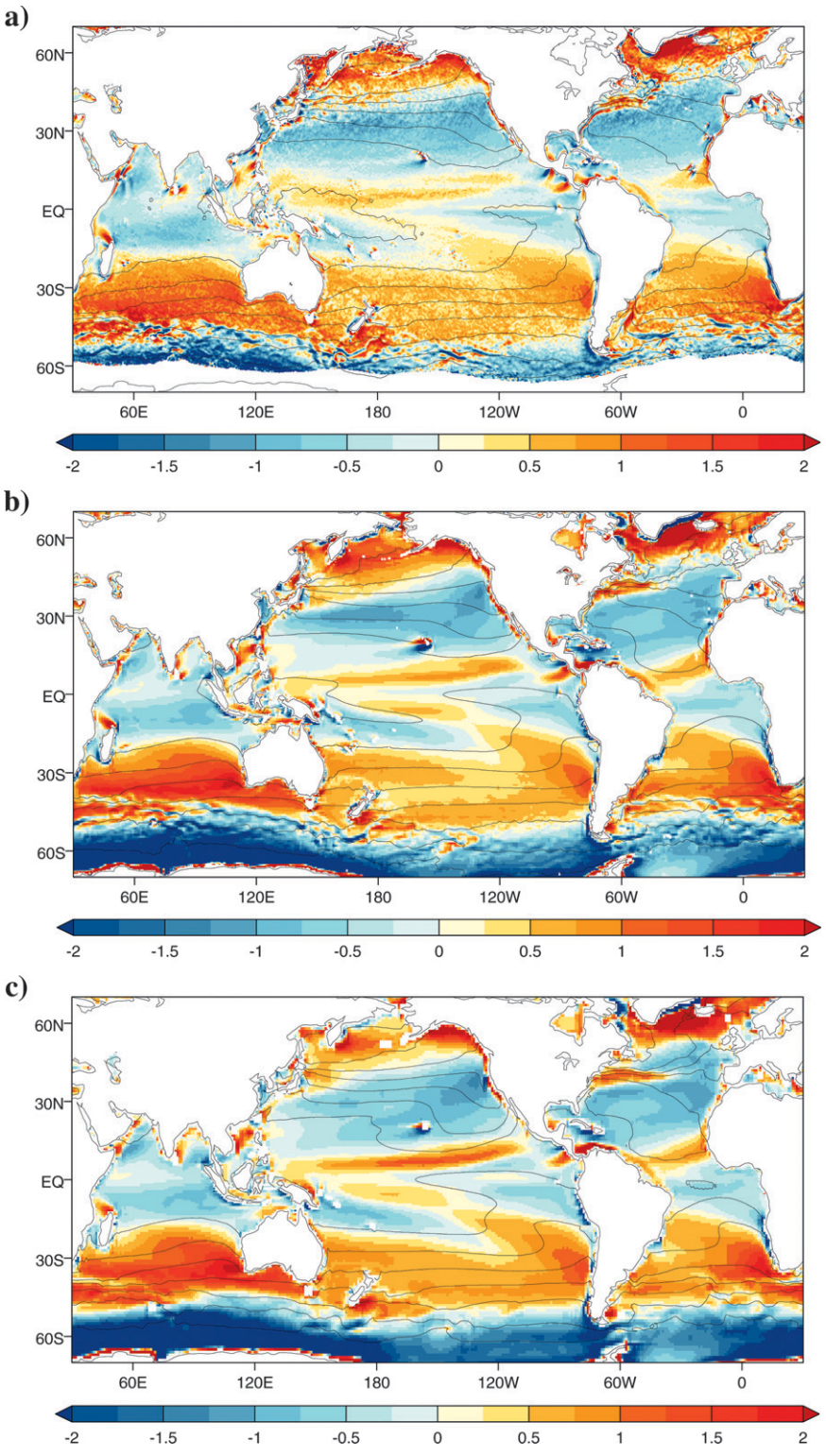

FIG. 22. Annual mean wind stress curl [N m^{-2} $(10^4$ km$)^{-1}$; colors] and SSTs (K; contours) from (a) QuikSCAT wind-stresses (from Risien and Chelton 2008) and 0.25° *WOA 2001* SSTs (Conkright et al. 2002), (b) 21–70-yr mean of HiGEM1.2 and (c) 21–70-yr mean of HadGEM1.2.

responses that affected the Antarctic Ocean circulation and the subsequent ability of the system to form seasonal sea ice. In the last decade or so of the simulation the sea ice is recovering, which provides an opportunity to analyze these feedbacks in more detail. It is interesting to note that the development of large multiyear polynyas is observed in the real system, for example, in the Weddell Sea during the 1970s, and it is possible that instabilities, such as those demonstrated by HiGEM, may be one way in which Antarctic sea ice may evolve in the future. This demonstrates again the importance of exploring high-resolution coupled processes to find out whether there are nonlinear feedbacks in the climate system that have hitherto been undetected in low-resolution models.

The development of HiGEM to produce a coupled model capable of stable multidecadal simulations presented a much bigger challenge than originally anticipated because of issues of numerical stability and computational performance. The computational resource required for such models is still at the limit of what is feasible for the long production runs required for climate change projections. However, there is sufficient computer power now for a systematic exploration of the importance of model resolution in the atmosphere and ocean, together, for simulating the coupled climate system. In the next phase of HiGEM the intention is to further increase the atmospheric resolution to bring it even closer to that of the ocean. It is only by undertaking these kinds of studies that the validity of lower-resolution climate models can be tested. At the same time, taking models to higher resolutions enables a much more meaningful comparison with the wealth of satellite data that exists on scales much finer than those currently used in models.

Acknowledgments. The support of NERC through the U.K. HiGEM project and the United Kingdom–Japan Climate Collaboration is acknowledged. The Met Office Hadley Centre also acknowledges the support of the United Kingdom–Japan Climate Collaboration through the Joint DEFRA and MoD Integrated Climate Programme GA01101, CBC/2B/0417-Annex C5.

This work made use of the facilities of HPCx, the U.K. Research Councils' national high-performance computing service, which is provided by EPCC at the University of Edinburgh and by CCLRC Daresbury Laboratory, and funded by the Office of Science and Technology through EPSRC's High End Computing Programme. Computing time at the Earth Simulator was kindly provided by JAMSTEC through the United Kingdom–Japan Climate Collaboration. Data archiving and distribution was provided by the British Atmospheric Data Centre. The CERES data were provided by Richard Allan and extracted from the NASA Atmospheric Data Services Center.

The authors would also like to thank Alison McLaren, Ann Keen, Manoj Joshi, and Thomas Toniazzo for their useful comments and support during the development of U.K. HiGEM, and the three anonymous reviewers whose comments contributed to improving this paper. This paper is dedicated to one of the authors, Anthony Slingo, who passed away before the publication of this manuscript. Tony's enthusiasm for environmental science was inspirational, and he will be sadly missed.

REFERENCES

Andres, R. J., and A. D. Kasgnoc, 1998: A time-averaged inventory of subaerial volcanic sulphur emissions. *J. Geophys. Res.,* **103,** 25 251–25 261.

AVISO, 1996: AVISO user handbook: Merged TOPEX/POSEIDON products. CNES, AVI-NT-02-101-CN, edition 3.0, 201 pp.

——, 1998: AVISO user handbook: Sea level anomalies (SLAs). CNES, AVI-NT-011-312-CN, edition 3.1, 24 pp.

Baringer, M. O., and J. E. Price, 1997: Mixing and spreading of the Mediterranean outflow. *J. Phys. Oceanogr.,* **27,** 1654–1677.

——, and J. C. Larsen, 2001: Sixteen years of Florida Current transport at 27°N. *Geophys. Res. Lett.,* **28,** 3179–3182.

Beckmann, A., and R. Doscher, 1997: A method for improved representation of dense water spreading over topography in geopotential-coordinate models. *J. Phys. Oceanogr.,* **27,** 581–591.

BODC, 2003: *Centenary Edition of the GEBCO Digital Atlas*. Published on behalf of the Intergovernmental Oceanographic Commission and the International Hydrographic Organization as part of the General Bathymetric Chart of the Oceans, British Oceanographic Data Centre, CD-ROM.

Bourke, R. H., and R. P. Garrett, 1987: Sea ice thickness distribution in the Arctic Ocean. *Cold Reg. Sci. Technol.,* **13,** 259–280.

Bryan, F. O., and W. R. Holland, 1989: A high-resolution simulation of the wind- and thermohaline-driven circulation of the North Atlantic Ocean. *Parameterization of Small-Scale Processes: Proc. 'Aha Huliko'a, Hawaiian Winter Workshop*, Honolulu, HI, University of Hawaii at Manoa, 99–115.

Chelton, D. B., and Coauthors, 2001: Observations of coupling between surface wind stress and sea surface temperature in the eastern tropical Pacific. *J. Climate,* **14,** 1479–1498.

——, M. G. Schlax, M. H. Freilich, and R. F. Milliff, 2004: Satellite measurements reveal persistent small-scale features in ocean winds. *Science,* **303,** 978–983.

Collins, W. J., D. S. Stevenson, C. E. Johnson, and R. G. Derwent, 1997: Tropospheric ozone in a global-scale three-dimensional Lagrangian model and its response to NOx emission controls. *J. Atmos. Chem.,* **26,** 223–274.

Comiso, J. C., 1999: Bootstrap sea ice concentrations for NIMBUS-7 SMMR and DMSP SSM/I. National Snow and Ice Data Center, Boulder, CO, digital media. [Available online at http://nsidc.org/data/nsidc-0079.html.]

Conkright, M. E., R. A. Locarnini, H. E. Garcia, T. D. O'Brien, T. P. Boyer, C. Stephen, and J. I. Antonov, 2002: *World Ocean Atlas 2001: Objective Analyses, Data Statistics, and Figures, CD-ROM Documentation*. National Oceanographic Data Center, Internal Rep. 17, 17 pp.

Cronin, M. F., S.-P. Xie, and H. Hashizume, 2003: Barometric pressure variations associated with eastern Pacific tropical instability waves. *J. Climate,* **16,** 3050–3057.

Cunningham, S. A., S. G. Alderson, B. A. King, and M. A. Brandon, 2003: Transport and variability of the Antarctic Circumpolar Current in the Drake Passage. *J. Geophys. Res.,* **108,** 8084, doi:10.1029/2001JC001147.

——, and Coauthors, 2007: Temporal variability of the Atlantic meridional overturning circulation at 26°N. *Science,* **317,** 935–938.

Davies, T., M. J. P. Cullen, A. J. Malcolm, M. H. Mawson, A. Staniforth, A. A. White, and N. Wood, 2005: A new dynamical core for the Met Office's global and regional modelling of the atmosphere. *Quart. J. Roy. Meteor. Soc.,* **131,** 1759–1782.

Dukowicz, J. K., and R. D. Smith, 1994: Implicit free surface method for the Bryan–Cox–Semtner ocean model. *J. Geophys. Res.,* **99,** 7991–8014.

Emanuel, K. A., 1994: *Atmospheric Convection*. Oxford University Press, 580 pp.

Fahrbach, E., J. Meincke, S. Österhus, G. Rohardt, U. Schauer, V. Tverberg, J. Verduin, and R. A. Woodgate, 2001: Direct measurements of heat and mass transports through the Fram Strait. *Polar Res.,* **20,** 217–224.

Feistel, R., and E. Hagen, 1995: On the Gibbs thermodynamic potential of seawater. *Prog. Oceanog.,* **36,** 249–327.

FRAM Group, 1991: An eddy-resolving model of the Southern Ocean. *Eos, Trans. Amer. Geophys. Union,* **72,** 169, 174–175.

Ganachaud, A., and C. Wunsch, 2003: Large-scale ocean heat and freshwater transports during the World Ocean Circulation Experiment. *J. Climate,* **16,** 696–705.

Gent, P. R., and J. C. McWilliams, 1990: Isopycnal mixing in ocean circulation models. *J. Phys. Oceanogr.,* **20,** 150–155.

Gill, A., 1982: *Atmosphere-Ocean Dynamics*. International Geophysics Series, Vol. 30, Academic Press, 662 pp.

Gordon, A. L., 2001: Interocean exchange. *Ocean Circulation and Climate: Observing and Modelling the Global Ocean*, G. Siedler, J. Church, and J. Gould, Eds., Academic Press, 303–314.

——, and J. C. Comiso, 1988: Polynyas in the Southern Ocean. *Sci. Amer.,* **256,** 90–97.

Gordon, C., C. Cooper, C. A. Senior, H. Banks, J. M. Gregory, T. C. Johns, J. F. B. Mitchell, and R. A. Wood, 2000: The simulation of SST, sea ice extents and ocean heat transports in a version of the Hadley Centre coupled model without flux adjustments. *Climate Dyn.,* **16,** 147–168.

Griffies, S. M., A. Gnanadesikan, R. C. Pacanowski, V. D. Larichev, J. K. Dukowicz, and R. D. Smith, 1998: Isoneutral diffusion in a z-coordinate ocean model. *J. Phys. Oceanogr.,* **28,** 805–830.

Guilyardi, E., 2006: El Niño–mean state-seasonal cycle interactions in a multi-model ensemble. *Climate Dyn.,* **26,** 329–348.

——, and Coauthors, 2004: Representing El Niño in coupled ocean–atmosphere GCMs: The dominant role of the atmospheric component. *J. Climate,* **17,** 4623–4629.

Hallberg, R., and A. Gnanadesikan, 2006: The role of eddies in determining the structure and response of the wind-driven Southern Hemisphere overturning: Results from the Modeling Eddies in the Southern Ocean (MESO) project. *J. Phys. Oceanogr.,* **36,** 2232–2252.

Han, Q., W. B. Rossow, and A. A. Lacis, 1994: Near-global survey of effective droplet radii in liquid water clouds using ISCCP data. *J. Climate,* **7,** 465–497.

Hansen, B., and S. Österhus, 2000: North Atlantic-Nordic Seas exchanges. *Prog. Oceanogr.,* **45,** 109–208.

Hashizume, H., S.-P. Xie, W. T. Liu, and K. Takeuchi, 2001: Local and remote atmospheric response to tropical instability waves: A global view from space. *J. Geophys. Res.,* **106,** 10 173–10 185.

Houldcroft, C., W. M. F. Grey, M. Barnsley, C. M. Taylor, S. O. Los, and P. R. J. North, 2009: New vegetation albedo parameters and global fields of soil background albedo derived from MODIS for use in a climate model. *J. Hydrometeor.,* **10,** 183–198.

Holland, D. M., 2001: An impact of subgrid-scale ice–ocean dynamics on sea ice cover. *J. Climate,* **14,** 1585–1601.

Hoskins, B. J., and D. J. Karoly, 1981: The steady linear response of a spherical atmosphere to thermal and orographic forcing. *J. Atmos. Sci.,* **38,** 1179–1196.

Huffman, G. J., and Coauthors, 2007: The TRMM Multisatellite Precipitation Analysis (TMPA): Quasi-global, multiyear, combined-sensor precipitation estimates at fine scale. *J. Hydrometeor.,* **8,** 38–55.

Hunke, E. C., and J. K. Dukowicz, 1997: An elastic-viscous-plastic model for sea ice dynamics. *J. Phys. Oceanogr.,* **27,** 1849–1867.

——, and W. H. Lipscomb, 2004: CICE: The Los Alamos Sea Ice Model, documentation and software, version 3.1. Los Alamos National Laboratory, LA-CC-98-16, 56 pp.

Johns, T. C., and Coauthors, 2006: The New Hadley Centre Climate Model (HadGEM1): Evaluation of coupled simulations. *J. Climate,* **19,** 1327–1353.

Johns, W. E., T. L. Townsend, D. M. Fratantoni, and W. B. Wilson, 2002: On the Atlantic inflow to the Caribbean Sea. *Deep-Sea Res.,* **49,** 211–243.

Jones, A., D. L. Roberts, M. J. Woodage, and C. E. Johnson, 2001: Indirect sulphate aerosol forcing in a climate model with an interactive sulphur cycle. *J. Geophys. Res.,* **106,** 20 293–20 310.

Jónsson, S., and J. Briem, 2003: Flow of Atlantic Water west of Iceland and onto the north Icelandic Shelf. *ICES Marine Science Symp.*, Vol. 219, Edinburgh, United Kingdom, ICES, 326–328.

Jung, T., S. K. Gulev, I. Rudeva, and V. Soloviov, 2006: Sensitivity of extratropical cyclone characteristics to horizontal resolution in the ECMWF model. *Quart. J. Roy. Meteor. Soc.,* **132,** 1839–1857.

K-1 Model Developers, 2004: K-1 coupled model (MIROC) description. Center for Climate System Research, University of Tokyo, K-1 Tech. Rep. 1, 34 pp.

Kettle, A. J., and Coauthors, 1999: A global database of sea-surface dimethylsulfide (DMS) measurements and a procedure to predict sea surface DMS as a function of latitude, longitude and month. *Global Biogeochem. Cycles,* **13,** 399–444.

Kiehl, J. T., and K. E. Trenberth, 1997: Earth's annual global mean energy budget. *Bull. Amer. Meteor. Soc.,* **78,** 197–208.

Kushnir, Y., W. A. Robinson, I. Blade, N. M. Hall, S. Peng, and R. T. Sutton, 2002: Atmospheric response to extratropical SST anomalies: A synthesis and evaluation of recent results. *J. Climate,* **15,** 2233–2256.

Le Traon, P. Y., F. Nadal, and N. Ducet, 1998: An improved mapping method of multisatellite altimeter data. *J. Atmos. Oceanic Technol.,* **15,** 522–534.

Linzden, R. S., and S. Nigam, 1987: On the role of sea surface temperature gradients in forcing low-level winds and convergence in the tropics. *J. Atmos. Sci.,* **44,** 2418–2436.

Lipscomb, W. H., 2001: Remapping the ice thickness distribution in sea ice models. *J. Geophys. Res.,* **106,** 13 989–14 000.

Loeb, N. G., and Coauthors, 2007: Multi-instrument comparison of top-of-atmosphere reflected solar radiation. *J. Climate,* **20,** 575–591.

Loveland, T. R., B. C. Reed, J. F. Brown, D. O. Ohlen, Z. Zhu, L. Yang, and J. W. Merchant, 2000: Development of a global land cover characteristics database and IGBP DISCover from 1 km AVHRR data. *Int. J. Remote Sens.,* **21,** 1303–1330.

Ma, C.-C., C. R. Mechoso, A. W. Robertson, and A. Arakawa, 1996: Peruvian stratus clouds and the tropical Pacific circulation—A coupled ocean–atmosphere GCM study. *J. Climate,* **9,** 1635–1645.

Macrander, A., U. Send, H. Valdimarsson, S. Jónsson, and R. H. Käse, 2005: Interannual changes in the overflow from the Nordic Seas into the Atlantic Ocean through Denmark Strait. *Geophys. Res. Lett.,* **32,** L06606, doi:10.1029/2004GL021463.

Maltrud, M. E., and J. L. McClean, 2005: An eddy resolving global 1/10° ocean simulation. *Ocean Modell.,* **8,** 31–54.

Marti, O., G. Madec, and P. Delecluse, 1992: Comment on ''Net diffusivity in Ocean General Circulation Models with Non-uniform grids'' by F. L. Lin and I. Y. Fung. *J. Geophys. Res.,* **97,** 12 763–12 766.

Martin, G. M., M. A. Ringer, V. D. Pope, A. Jones, C. Dearden, and T. J. Hinton, 2006: The physical properties of the atmosphere in the new Hadley Centre Global Environmental Model (HadGEM1). Part I: Model description and global climatology. *J. Climate,* **19,** 1274–1301.

McDougall, T. J., D. R. Jackett, D. G. Wright, and R. Feistel, 2003: Accurate and computationally efficient algorithms for potential temperature and density of seawater. *J. Atmos. Oceanic Technol.,* **20,** 730–741.

McLaren, A. J., and Coauthors, 2006: Evaluation of the sea ice simulation in a new coupled atmosphere-ocean climate model (HadGEM1). *J. Geophys. Res.,* **111,** C12014, doi:10.1029/2005JC003033.

Naveira Garabato, A. C., D. P. Stevens, and K. J. Heywood, 2003: Water mass conversion, fluxes, and mixing in the Scotia Sea diagnosed by an inverse model. *J. Phys. Oceanogr.,* **33,** 2565–2587.

New, M., D. Lister, M. Hulme, and I. Makin, 2002: A high-resolution data set of surface climate over global land areas. *Climate Res.,* **21,** 1–25.

Pacanowski, R. C., and S. M. Griffies, 1998: MOM3.0 manual. NOAA/GFDL, 692 pp.

Pope, V. D., and R. A. Stratton, 2002: The processes governing horizontal resolution sensitivity in a climate model. *Climate Dyn.,* **19,** 211–236.

Rahmstorf, S., 1993: A fast and complete convection scheme for ocean models. *Ocean Modell.,* **101,** 9–11.

Randel, W. J., and F. Wu, 1999: A stratospheric ozone trends data set for global modelling studies. *Geophys. Res. Lett.,* **26,** 3089–3092.

Ringer, M. A., and Coauthors, 2006: The physical properties of the atmosphere in the new Hadley Centre Global Environmental Model (HadGEM1). Part II: Aspects of variability and regional climate. *J. Climate,* **19,** 1302–1326.

Risien, C. M., and D. B. Chelton, 2008: A global climatology of surface wind and wind stress fields from 8 years of QuikSCAT scatterometer data. *J. Phys. Oceanogr.,* **38,** 2379–2413.

Roberts, M. J., and D. Marshall, 1998: Do we require adiabatic dissipation schemes in eddy-resolving ocean models? *J. Phys. Oceanogr.,* **28,** 2050–2063.

——, and Coauthors, 2004: Impact of an eddy-permitting ocean resolution on control and climate change simulations with a global coupled GCM. *J. Climate*, **17,** 3–20.

——, J. Donners, J. Harle, and I. Stevens, 2008: Impact of relative atmosphere-ocean resolution on coupled climate models. *CLIVAR Exchanges*, No. 44, International CLIVAR Project Office, Southampton, United Kingdom, 8–11.

——, and Coauthors, 2009: Impact of resolution on the tropical Pacific circulation in a matrix of coupled models. *J. Climate*, in press.

Rundick, D. L., 1997: Direct velocity measurements in the Samoan Passage. *J. Geophys. Res.,* **102,** 3293–3302.

Russell, J. L., R. J. Stouffer, and K. W. Dixon, 2006: Intercomparison of the Southern Ocean circulations in IPCC coupled model control simulations. *J. Climate,* **19,** 4560–4575.

Sakamoto, T. T., A. Sumi, S. Emori, T. Nishimura, H. Hasumi, T. Suzuki, and M. Kimoto, 2004: Far-reaching effects of the Hawaiian Islands in the CCSR/NIES/FRCGC high-resolution climate model. *Geophys. Res. Lett.,* **31,** L17212, doi:10.1029/2004GL020907.

Sardeshmukh, P. D., and B. J. Hoskins, 1988: On the generation of global rotational flow by steady idealized tropical divergence. *J. Atmos. Sci.,* **45,** 1228–1251.

Semtner, A. J., 1976: A model for the thermodynamic growth of sea ice in numerical investigations of climate. *J. Phys. Oceanogr.,* **6,** 379–389.

——, and R. M. Chervin, 1988: A simulation of the global ocean circulation with resolved eddies. *J. Geophys. Res.,* **93,** 15 502–15 522.

——, and ——, 1992: Ocean general circulation from a global eddy-resolving model. *J. Geophys. Res.,* **97,** 5493–5550.

Slingo, J. M., P. M. Inness, R. B. Neale, S. J. Woolnough, and G.-Y. Yang, 2003: Scale interactions on diurnal to seasonal timescales and their relevance to model systematic errors. *Ann. Geophys.,* **46,** 139–155.

Small, J., S.-P. Xie, and Y. Wang, 2003: Numerical simulation of the atmospheric response to Pacific tropical instability waves. *J. Climate,* **16,** 3722–3740.

Smith, R. D., M. E. Maltrud, F. O. Bryan, and M. W. Hect, 2000: Numerical simulation of the North Atlantic Ocean at 1/10°. *J. Phys. Oceanogr.,* **30,** 1532–1561.

Smith, S. J., R. Andres, E. Conception, and J. Lurz, 2004: Historical sulfur dioxide emissions 1850–2000: Methods and results. Joint Global Change Research Institute, PNNL Rep. 14537, 13 pp.

Smith, W. H. F., and D. Sandwell, 1997: Global seafloor topography from satellite altimetry and ship depth soundings. *Science,* **277,** 1956–1962.

Solomon, S., D. Qin, M. Manning, Z. Chen, M. Marquis, K. B. Averyt, M. Tignor, and H. L. Miller, Eds., 2007: *Climate Change 2007: The Physical Science Basis*. Cambridge University Press, 996 pp.

Spencer, H., and J. M. Slingo, 2002: The simulation of peak and delayed ENSO teleconnections. *J. Climate,* **16,** 1757–1774.

Spiro, P. A., D. J. Jacob, and J. A. Logan, 1992: Global inventory of sulfur emissions with 1° × 1° resolution. *J. Geophys. Res.,* **97,** 6023–6036.

Strachan, J., 2007: Understanding and modelling the climate of the maritime continent. Ph.D. thesis, University of Reading, 220 pp.

Sutton, R. T., W. A. Norton, and S. P. Jewson, 2001: The North Atlantic Oscillation—What role for the ocean? *Atmos. Sci. Lett.,* **1,** 89–100.

Taylor, C. M., D. J. Parker, and P. P. Harris, 2007: An observational case study of mesoscale atmospheric circulations induced by soil moisture. *Geophys. Res. Lett.,* **34,** L15801, doi:10.1029/2007GL030572.

Thompson, S. R., 1995: Sills of the global ocean: A compilation. *Ocean Modell.,* **109,** 7–9.

Timmermann, R., P. Lemke, and C. Kottmeier, 1999: Formation and maintenance of a polynya in the Weddell Sea. *J. Phys. Oceanogr.,* **29,** 1251–1264.

Trenberth, K. E., and J. M. Caron, 2001: Estimates of meridional atmosphere and ocean heat transports. *J. Climate,* **14,** 3433–3443.

——, L. Smith, T. Qian, A. Dai, and J. Fasullo, 2007: Estimates of the global water budget and its annual cycle using observational and model data. *J. Hydrometeor.,* **8,** 758–769.

Visbeck, M., J. Marshall, T. Haine, and M. Spall, 1997: Specification of eddy transfer coefficients in coarse-resolution ocean circulation models. *J. Phys. Oceanogr.,* **27,** 381–402.

Wajsowicz, R. C., 2002: A modified Sverdrup model of the Atlantic and Caribbean circulation. *J. Phys. Oceanogr.,* **32,** 973–993.

Wallace, J. M., T. P. Mitchell, and C. Deser, 1989: The influence of sea surface temperature on surface wind in the eastern equatorial Pacific: Seasonal and interannual variability. *J. Climate,* **2,** 1492–1499.

Webster, S., A. R. Brown, D. R. Cameron, and C. P. Jones, 2003: Improvements to the representation of orography in the Met Office Unified Model. *Quart. J. Roy. Meteor. Soc.,* **129,** 1989–2010.

Woodgate, R. A., K. Aagaard, and T. Weingartner, 2005: Monthly temperature, salinity, and transport variability of the Bering Strait through flow. *Geophys. Res. Lett.,* **32,** L04601, doi:10.1029/2004GL021880.

Wild, M., and E. Roeckner, 2006: Radiative fluxes in the ECHAM5 general circulation model. *J. Climate,* **19,** 3792–3809.

Xie, P., and P. Arkin, 1997: Global precipitation: A 17-year monthly analysis based on gauge observations, satellite estimates, and numerical model outputs. *Bull. Amer. Meteor. Soc.,* **78,** 2539–2558.